# Déformation, hydratation et anisotropie du manteau lithosphérique sous un rift actif

Le rifting est un processus complexe entraînant l'amincissement d'une plaque continentale. Bien que le manteau représente plus de 60% de la lithosphère, peu de choses sont connues sur le rôle du manteau sur l'initiation du rifting, mais aussi sur la façon dont le manteau accommode la déformation durant le rifting. Vauchez et al. (1997) et Tommasi et Vauchez (2001) suggérèrent que l'extension continental se produit sous un régime de déformation en transtension produit par la réactivation d'ancienne OPR de l'olivine préservée dans la lithosphère. En plus de subir à des forces extensives, la lithosphère est soumise à une percolation extensive de magmas. Buck (2006) proposa ainsi que l'intrusion de filons pourrait aider à initier l'extension au cœur de la lithosphère continentale.

Le travail présenté dans ce chapitre repose sur l'analyse de 53 xénolites mantelliques de la Divergence Nord Tanzanienne provenant de 4 localités différentes : deux au cœur du rift Est-Africain (Pello Hill et Eledoi) et deux au cœur de la ceinture volcanique transverse (Lashaine et Olmani). Cette étude est basée sur la caractérisation des microstructures, des OPRs, des teneurs en hydrogène dans l'olivine des xénolites tanzaniens, ainsi que sur le calcul de leurs propriétés sismiques. Elle vise à mieux comprendre les relations entre déformation et percolation de fluides et magmas au début du rifting ainsi que son régime de déformation.

L'analyse de ces échantillons révèle une variation significative des microstructures et des OPRs en fonction de leur provenance. Au cœur du rift, les microstructures porphyroclastiques et mylonitiques enregistrent une déformation par fluage dislocation récente, ainsi que de fortes variations de température. Les cristaux d'orthopyroxène très étirés dans les mylonites suggèrent une initiation de la déformation à faible contrainte et probablement basse température. Le remplacement de l'orthopyroxène par l'olivine dans les péridotites porphyroclastiques et mylonitiques indique des réactions magmas-roches syn-cinématiques et une déformation se poursuivant sous des conditions proches du solidus.

Enfin, les exsolutions dans les orthopyroxènes suggèrent un refroidissement important avant extraction des xénolites. Les OPRs de l'olivine de type axial-[100] et l'orientation des directions de polarisation des ondes SKS suggère que le rift s'est formé sous un régime en transtension (Vauchez et al., 2000).

Au cœur de la ceinture volcanique transverse, à Lashaine, les microstructures granulaires à gros grains indiquent une déformation par fluage dislocation à faibles contraintes déviatoriques suivie par du recuit. Les OPRs de l'olivine de type orthorhombique à axial-[010] peuvent être associées à la formation de la chaîne Mozambique ou un événement plus ancien (probablement Archéen, Gibson et al., 2013). A Olmani, des microstructures et des OPRs intermédiaires sont observées, suggérant une déformation hétérogène au sein de la ceinture volcanique transverse, probablement lié au développement du graben de Pangani.

Les teneurs en hydrogène dans l'olivine sont comprises entre 2 et 18 ppm wt. $H_2O$, mais ne varient pas en fonction de la localité, de la microstructure ou du type d'OPR. La présence d'hydrogène dans l'olivine au Mg# élevé suggère une réhydration par métasomatisme. Toutefois, l'absence de corrélation spatiale entre les veines tardives et les teneurs en hydrogène dans l'olivine et l'absence de profil de diffusion dans l'olivine indiquent que l'hydratation de ces échantillons n'a eu lieu ni durant cet épisode métasomatique, ni durant l'extraction des xénolites à la surface.

# Deformation, hydration, and anisotropy of the lithospheric mantle in an active rift: constraints from mantle xenoliths from the North Tanzanian Divergence of the East African Rift

Virginie Baptiste[1], Alain Vauchez[1], Andréa Tommasi[1], Sylvie Demouchy[1] and Roberta L. Rudnick[2]

[1]*Géosciences Montpellier, Université Montpellier 2 & CNRS, CC 60, Place E. Bataillon, 34095 Montpellier cedex 5, France.*
[2] *Department of Geology, University of Maryland, College Park, Maryland 20742, USA.*

*Running title: Deformation of the mantle lithosphere in an active rift*

(*) corresponding author: virginie.baptiste@gm.univ-montp2.fr;
Phone: +33 467144912
Fax: +33 467143603

**Abstract**

We have analyzed the microstructures and crystal preferred orientations (CPO) and calculated the seismic properties of 53 mantle xenoliths from 4 localities within the North Tanzanian Divergence of the East African rift: 2 within the rift axis and 2 in the transverse volcanic belt. Olivine OH concentrations were measured in fifteen xenoliths. Most samples have harzburgitic to dunitic compositions and high olivine Mg#. Microstructures and olivine CPO patterns vary strongly depending on the location. In-axis peridotites display mylonitic to porphyroclastic microstructures, which record recent deformation by dislocation creep. Highly stretched orthopyroxenes in mylonites indicate that the deformation was initiated under high stress and probably low temperature. Orthopyroxene replacement by olivine in mylonitic and porphyroclastic peridotites suggest synkinematic melt-rock reactions and further deformation under near-solidus conditions. Exsolutions in orthopyroxene imply significant cooling between melt-assisted deformation and xenolith extraction. Late hydrous metasomatism is evidenced by the occurrence of veins crosscutting the microstructure and interstitial clinopyroxene and phlogopite. Axial-[100] olivine CPOs predominate, suggesting activation of the high temperature, low pressure [100]{0kl} slip systems and, probably, transtensional deformation. In the volcanic belt, Lashaine peridotites display very coarse-granular textures, indicating deformation by dislocation creep under low deviatoric stress conditions followed by annealing. They have orthorhombic to axial-[010] olivine CPO symmetries. The latter are consistent with activation of the [001](010) slip system in addition to the dominant [100](010) system and may result from transpressional deformation. Intermediate microstructures and CPOs in Olmani suggest heterogeneous deformation within the volcanic belt. Olivine OH concentrations range between 2 and 12 ppm wt. $H_2O$. No systematic variations are observed between in- and off-axis samples. Maximum P wave azimuthal anisotropy (AVp) ranges between 3.3 and 18.4%, and the maximum S wave polarization anisotropy (AVs) between 2.3 and 13.2%. Comparison between seismic properties of in-axis peridotites and SKS splitting data suggests transtensional deformation in the lithospheric mantle beneath the rift.

# 1. Introduction

Continental rifting is a complex process that results in localized thinning and, in some cases, in disruption of a continental plate. While the surface expression of this deformation is clear and usually well understood, little is known about how the lithospheric mantle deforms to accommodate rifting. The widely differing surface expression of continental rifting has led to contrasting lithospheric extension models. McKenzie (1978) proposed a symmetrical rift model, where the lithosphere deforms by homogeneous thinning and stretching in response to far field extensional forces. To account for the observations in the Basin and Range, Wernicke (1981, 1985) proposed an asymmetrical extension model, in which the deformation is localized on a lithospheric-scale detachment fault. However, such models cannot account for the narrow rift valley and the strong mantle lithosphere thinning observed in East Africa (Dugda et al., 2007, 2009). The latter observations are in better agreement with the Nicolas et al. (1994) model, where rifting occurs via lithospheric rupture and rise of an asthenospheric wedge within the lithospheric mantle. The later model has been further developed by Vauchez et al. (1997) and Tommasi and Vauchez (2001), who, based on the analysis of the influence of inherited structures on the localization of continental breakup, suggested that most major rifts start forming through a transtensional deformation regime produced by the reactivation of the olivine crystallographic fabric frozen in the lithospheric mantle. Numerical models in which the upper mantle has an anisotropic viscosity controlled by the evolution of olivine crystallographic orientations corroborate this assumption (Tommasi et al., 2009). Rheological heterogeneities, both in the crust and in the mantle, also have a major effect on the localization of rifting (e.g., Dunbar and Sawyer, 1989; Nyblade and Brazier, 2002; Vauchez et al., 1997).

In addition to being deformed by an extensional regime, the lithosphere within an active rift is often subjected to extensive magma percolation. Dyke intrusions have been proposed to help initiate extension in a thick continental lithosphere (Buck, 2006). The major role of magmas in rifting has been corroborated by seismic anisotropy data in the Afars, which unambiguously point to aligned melt pockets throughout the crust and lithospheric mantle (Bastow et al. 2010; Kendall et al. 2005). At a smaller scale, the presence of melt may result in weakening of mantle rocks (Hirth and Kohlstedt, 2003; Zimmerman and Kohlstedt, 2004). It may trigger strain localization if melt is heterogeneously distributed (e.g., Le Roux et al., 2008) or promote homogeneous deformation if it is homogeneously distributed through a large volume (Vauchez et al., 2012). Melt- or fluid-rock reaction may also result in

softening through crystallization of weaker phases and/or associated grain size reduction and phase mixing (e.g., Dijkstra et al. 2002; Soustelle et al. 2010).

Mantle xenoliths provide a valuable means by which to study the deformation of mantle lithosphere during rifting. They allow for quantification of the hydration state and characterization of melt-rock reactions and of their timing relative to the deformation. Moreover, the analysis of the microstructures and crystallographic preferred orientations (CPO) bring constraints on the deformation mechanisms and conditions in the lithospheric mantle below active rifts. In the present study, we explore the relations between deformation, melt or fluids percolation, and hydration in a series of mantle xenoliths from four localities in the North Tanzanian Divergence region (East African Rift). This region, still in the early stages of rifting, offers favorable conditions to study the expression of rifting on the lithospheric mantle. In addition, we estimate the seismic anisotropy of these rocks based on their CPO and mineralogical composition and compare these results to seismic anisotropy measurements performed within and around the East African Rift.
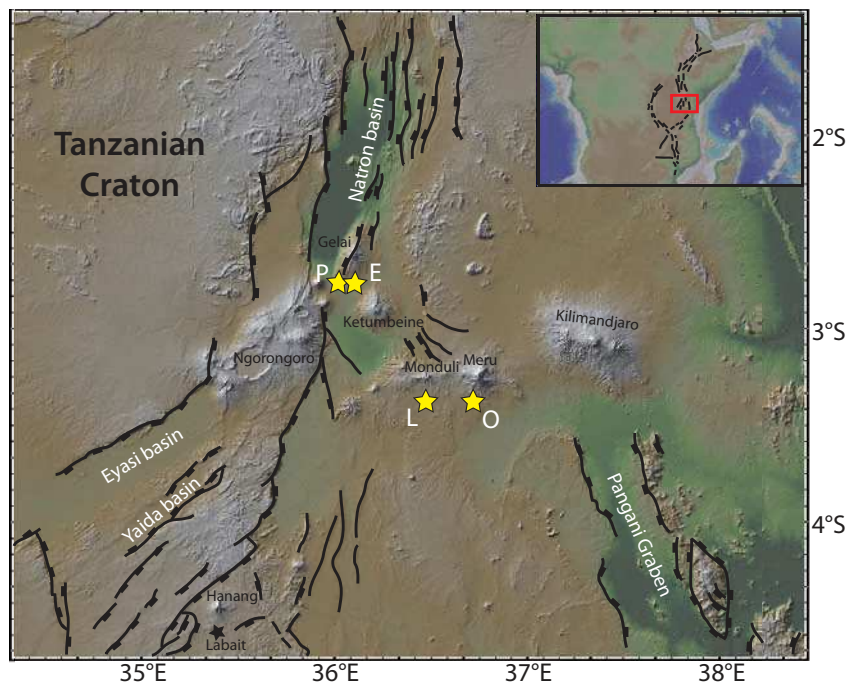


Figure 1: Digital topographic map (http://www.geomapapp.org, topography data from Ryan et al., 2009) showing the North Tanzania Divergence and the location of the xenolith localities studied here (P: Pello Hill, E: Eledoi, L: Lashaine, and O: Olmani), as well as the Tanzania craton and main volcanoes. Major volcanoes are labeled. Labait is another locality containing abundant mantle xenoliths, which microstructures and crystal preferred orientations were studied by Vauchez et al. (2005).

## 2. Geological setting

The East African Rift is one of the few active continental rifts on Earth. It extends over ~ 4000 km, from the Afar triple junction in the Red Sea to the Gulf of Mozambique (Fig. 1), mostly following the trend of older orogenic belts (Nyblade and Brazier, 2002; Vauchez et al., 1997 and references therein). Rifting and volcanism started 35 Ma ago in Ethiopia and northern Kenya (MacDonald et al., 2001; Morley et al., 1992) in a lithosphere stabilized since the Neoproterozoic. It migrated southwards, reaching southern Kenya 8-5 Ma ago (Cerling and Powers, 1977; Crossley and Knight, 1981). The youngest section of the East African Rift splits into two branches around the Tanzania craton. In the Eastern branch, extension is accompanied by intense magmatic activity concentrated within the rift valley. The region experiences relatively intense present-day seismic activity, with earthquakes mainly located within the rift valley or in its immediate surroundings (e.g., Albaric et al., 2010; Nyblade et al., 1996). A major faulting episode at $1.0 \pm 0.2$ Ma (MacIntyre et al., 1974) gave rise to the present-day rift valley morphology. In addition, off-axis volcanic activity is observed in the North Tanzanian Divergence, south of which rifting occurs in a more diffuse manner, with deformation accommodated in many branches (Figure 1). Seismic studies show that crustal and lithospheric thicknesses in this young rifting domain vary between 36-44 km and 100-150 km, respectively (Dugda et al., 2009; Julià et al., 2005).

Mantle xenoliths occur in both in- and off-axis volcanoes, providing an exceptional opportunity to study the tectono-thermal evolution of the mantle lithosphere in response to the progression of the East African Rift along the boundary between the Tanzanian craton and the N¬eoproterozoic Mozambique Belt. The present study focuses on 53 mantle xenoliths from four localities from the North Tanzanian Divergence (Fig. 1): two within the rift valley (Pello Hill and Eledoi) and two within the transverse volcanic belt (Lashaine and Olmani). The xenoliths from the cratered tuff cone of Pello Hill and from the Eledoi explosion crater were collected in fine-grained scoria with a bulk-rock chemistry similar to olivine-melilitites and olivine-nephelinites (Dawson and Smith, 1988). The formation of these craters postdates the major rift faulting episode at 1.2 Ma (Dawson and Smith, 1988). The Lashaine tuff cone and the Olmani cinder cone are ankaramite rift-related volcanoes erupted during the Neogene. They are located in a part of the Mozambique Belt characterized by Archean crustal material reworked in the Neoproterozoic by the Mozambique orogeny (Mansur et al., 2014 and references therein; Möller et al., 1998).

Table 1: Texture, equilibrium temperatures, olivine Mg#, modal contents, olivine CPO, olivine J-index, olivine BA index, and calculated density and seismic properties of the studied Tanzanian peridotites.

| Locality | Sample | Thin section | Texture | Temperature | Ol mg# | Opx mg# | Reference for mg# and T data | Modal compositions* (%) | | | | | | Olivine CPO type | Olivine J-index | Olivine BA index | Density | Max AVp | Max AVs pol | Max AVS$_1$ | Max AVS$_2$ |
|---|---|---|---|---|---|---|---|---|---|---|---|---|---|---|---|---|---|---|---|---|---|
| | | | | (°C) | (%) | (%) | | ol | opx | cpx | gt | phl | amph | | | | (g.cm$^{-3}$) | (%) | (%) | (%) | (%) |
| Eledoi | EL3 | EL3 | P | 1068 | 92.1 | 92.5 | This study | 88 | 11 | 1 | 0 | 0 | 0 | Axial-[100] to ortho | 3.31 | 0.73 | 3.3493 | 9.0 | 6.1 | 3.0 | 5.1 |
| | EL6 | EL6 | P | - | 90.3 | - | LCT01 | 98 (86) | 2 (2) | 0 (10) | 0 (0) | 0 (2) | 0 (0) | Axial-[100] to ortho | 4.63 | 0.78 | 3.3401 | 10.7 | 7.0 | 3.5 | 5.6 |
| | EL8 | EL8 | P | 1063 | 92.4 | 93.3 | This study | 92 | 6 | 2 | 0 | 0 | 0 | Axial-[100] | 3.82 | 0.78 | 3.3515 | 11.4 | 8.1 | 3.8 | 6.2 |
| | EL10 | EL10 | P | - | 92.4 | - | LCT01 | 97 | 1 | 2 | 0 | 0 | 0 | Ortho | 3.15 | 0.62 | 3.3540 | 9.4 | 5.8 | 2.8 | 5.5 |
| | EL11 | EL11 | P | - | 90.8 | - | LCT01 | 92 | 7 | 1 | 0 | 0 | 0 | Axial-[100] | 2.88 | 0.69 | 3.3515 | 8.8 | 5.6 | 3.2 | 4.2 |
| | EL12 | EL12 | P | 1060 | 91.8 | 92.5 | This study | 88 | 10 | 2 | 0 | 0 | 0 | Axial-[100] | 4.34 | 0.90 | 3.3495 | 11.2 | 7.6 | 3.4 | 6.0 |
| | EL14 | EL14 | CG | - | 84.1 | - | LCT01 | 100 (93) | 0 (0) | 0 (4) | 0 (0) | 0 (3) | 0 (0) | Axial-[100] | 4.46 | 0.87 | 3.3372 | 9.4 | 3.1 | 3.1 | 6.0 |
| | EL15 | EL15 | P | 1052 | 90.1 | 91.5 | This study | 85 (61) | 15 (11) | 0 (23) | 0 | 0 (5) | 0 | Axial-[100] | 3.31 | 0.74 | 3.3154 | 4.1 | 3.9 | 3.3 | 1.8 |
| | EL16 | EL16 | P | - | 92.1 | - | LCT01 | 91 | 0 | 9 | 0 | 0 | 0 | Axial-[100] | 2.14 | 0.84 | 3.3525 | 7.5 | 4.9 | 1.6 | 4.5 |
| Pello Hill | PEL1 | PEL1 | P | - | 88.4 | - | LCT01 | 95 | 4 | 1 | 0 | 0 | 0 | Ortho | 3.38 | 0.84 | 3.3528 | 9.9 | 6.3 | 2.9 | 5.4 |
| | PEL7 | PEL7 | P | - | 92.3 | 92.9 | This study | 86 | 13 | 1 | 0 | 0 | 0 | Ortho | 5.38 | 0.70 | 3.3484 | 12.3 | 8.0 | 4.1 | 6.6 |
| | PEL9 | PEL9 | P | - | 93.3 | - | LCT01 | 96 (95) | 4 (4) | 0 (0) | 0 (0) | 0 (1) | 0 (0) | Axial-[100] | 4.77 | 0.87 | 3.3475 | 12.2 | 8.2 | 5.0 | 6.1 |
| | | PEL9-bis | P | - | - | - | | 93 | 7 | 0 | 0 | 0 | 0 | Axial-[100] | 4.71 | 0.90 | 3.3516 | 12.0 | 7.9 | 4.3 | 6.2 |
| | PEL11 | PEL11 | CG | - | 86.7 | - | LCT01 | 100 | 0 | 0 | 0 | 0 | 0 | Ortho | 3.27 | 0.45 | 3.3550 | 4.8 | 4.9 | 3.6 | 2.1 |
| | PEL12 | PEL12A | P | - | 92.6 | - | LCT01 | 83 (78) | 16 (15) | 1 (1) | 0 (0) | 0 (1) | 0 (5) | Axial-[100] | 3.40 | 0.86 | 3.3276 | 8.7 | 5.9 | 2.3 | 5.0 |
| | | PEL12B | P | - | - | - | | 82 (77) | 17 (16) | 1 (1) | 0 (0) | 0 (2) | 0 (4) | Axial-[100] | 3.16 | 0.89 | 3.3244 | 8.3 | 5.6 | 3.0 | 4.6 |
| | PEL15 | PEL15 | M | - | 92.4 | 92.9 | LCT01 | 77 | 21 | 2 | 0 | 0 | 0 | Ortho | 3.64 | 0.61 | 3.3441 | 7.4 | 5.5 | 3.1 | 4.2 |
| | PEL16 | PEL16 | P | - | 92.5 | 93.2 | LCT01 | 90 | 9 | 1 | 0 | 0 | 0 | Axial-[100] to ortho | 6.69 | 0.82 | 3.3506 | 13.5 | 8.9 | 5.0 | 6.6 |
| | PEL17 | PEL17 | M | - | 92.4 | 92.6 | LCT01 | 87 (86) | 12 (12) | 1 (1) | 0 (0) | 0 (0) | 0 (1) | Axial-[100] | 4.71 | 0.79 | 3.3434 | 9.6 | 6.5 | 2.1 | 6.1 |
| | | PEL17A | M | - | - | - | | 76 (75) | 23 (23) | 1 (1) | 0 (0) | 0 (0) | 0 (1) | Axial-[100] | 3.29 | 0.84 | 3.3434 | 9.6 | 6.5 | 2.1 | 6.1 |
| | | PEL17B | M | - | - | - | | 75 (74) | 25 (25) | 0 (0) | 0 (0) | 0 (0) | 0 (1) | Axial-[100] | 4.23 | 0.79 | 3.3428 | 9.7 | 6.9 | 2.7 | 5.9 |
| | PEL20 | PEL20 | P | - | 92.3 | - | LCT01 | 97 | 0 | 3 | 0 | 0 | 0 | Ortho | 3.79 | 0.69 | 3.3542 | 9.0 | 7.3 | 3.8 | 6.1 |
| | PEL21 | PEL21A | P | - | 91.3 | - | LCT01 | 100 (84) | 0 (0) | 0 (8) | 0 (0) | 0 (0) | 0 (8) | Axial-[100] | 3.20 | 0.78 | 3.3300 | 10.0 | 6.5 | 3.1 | 5.2 |
| | | PEL21B | P | - | - | - | | 100 (86) | 0 (0) | 0 (8) | 0 (0) | 0 (1) | 0 (5) | Axial-[100] | 3.31 | 0.81 | 3.3330 | 9.4 | 6.2 | 3.1 | 5.1 |
| | PEL22 | PEL22A | P | 1090 | 91.5 | 91.6 | This study | 96 (90) | 4 (4) | 0 (5) | 0 (0) | 0 (0) | 0 (1) | Axial-[100] to ortho | 4.26 | 0.70 | 3.3488 | 11.0 | 7.1 | 4.0 | 5.3 |
| | | PEL22B | P | - | - | - | | 95 (88) | 5 (5) | 0 (6) | 0 (0) | 0 (0) | 0 (1) | Axial-[100] to ortho | 4.21 | 0.70 | 3.3457 | 10.5 | 7.0 | 3.9 | 5.2 |
| | PEL27 | PEL27 | P | - | 92.3 | - | LCT01 | 95 | 0 | 5 | 0 | 0 | 0 | Axial-[100] to ortho | 3.76 | 0.79 | 3.3536 | 11.8 | 7.5 | 3.5 | 6.5 |
| | PEL33 | PEL33 | P | 1090 | 92.4 | 93.1 | This study | 83 | 16 | 1 | 0 | 0 | 0 | Axial-[100] | 3.79 | 0.64 | 3.3469 | 9.1 | 6.5 | 3.8 | 4.8 |
| | PEL34 | PEL34A | P | - | 92.4 | - | LCT01 | 86 (85) | 12 (12) | 2 (2) | 0 (0) | 0 (0) | 0 (1) | Axial-[100] | 4.01 | 0.89 | 3.3457 | 10.8 | 7.2 | 3.0 | 6.1 |
| | | PEL34B | P | - | - | - | | 86 (85) | 13 (13) | 1 (1) | 0 (0) | 0 (0) | 0 (1) | Axial-[100] | 4.17 | 0.91 | 3.3455 | 10.6 | 7.0 | 2.9 | 6.1 |
| | PEL38 | PEL38 | P | - | 91.2 | - | LCT01 | 93 (92) | 7 (7) | 0 (0) | 0 (0) | 0 (0) | 0 (1) | Axial-[100] | 4.99 | 0.83 | 3.3516 | 11.3 | 7.6 | 3.6 | 6.3 |
| | PEL39 | PEL39 | P | - | 90.1 | - | LCT01 | 100 (78) | 0 (0) | 0 (21) | 0 (0) | 0 (1) | 0 (0) | Axial-[100] | 3.16 | 0.90 | 3.3436 | 7.8 | 4.5 | 2.5 | 3.4 |
| | PEL40 | PEL40A | P | - | 91.0 | - | LCT01 | 89 (75) | 11 (9) | 0 (12) | 0 (0) | 0 (3) | 0 (1) | Ortho | 4.55 | 0.66 | 3.3277 | 10.0 | 7.6 | 5.0 | 5.5 |
| | | PEL40B | P | - | - | - | | 88 (76) | 12 (10) | 0 (12) | 0 (0) | 0 (1) | 0 (1) | Ortho | 4.71 | 0.69 | 3.3383 | 10.2 | 7.1 | 4.0 | 5.7 |
| | PEL41 | PEL41 | CG | - | 87.9 | - | LCT01 | 100 (79) | 0 (0) | 0 (15) | 0 (0) | 0 (3) | 0 (3) | Axial-[100] | 3.16 | 0.79 | 3.3256 | 6.4 | 4.9 | 1.8 | 4.4 |

Table 1 (suite)

| Locality | Sample | Thin section | Texture | Temperature (°C) | Ol mg# (%) | Opx mg# (%) | Reference for mg# and T data | ol | opx | cpx | gt | phl | amph | Olivine CPO type | Olivine J-index | Olivine BA index | Density (g.cm$^{-3}$) | Max AVp (%) | Max AVs pol (%) | Max AVS$_1$ (%) | Max AVS$_2$ (%) |
|---|---|---|---|---|---|---|---|---|---|---|---|---|---|---|---|---|---|---|---|---|---|
| Lashaine | 89-664 | 89-664 | VCG | - | - | - | - | 93 | 7 | 0 | 0 | 0 | 0 | Axial-[010] to ortho | 5.97 | 0.67 | 3.3518 | 8.0 | 6.5 | 2.8 | 4.9 |
| | | 89-664A | VCG | 1075 | 90.2 | 91.0 | This study | 85 | 13 | 2 | 0 | 0 | 0 | Axial-[010] to ortho | 5.47 | 0.66 | 3.3484 | 5.9 | 4.5 | 2.6 | 3.8 |
| | | 89-664B | VCG | - | - | - | - | 94 | 5 | 1 | 0 | 0 | 0 | Axial-[010] to ortho | 5.42 | 0.66 | 3.3523 | 6.8 | 5.1 | 1.7 | 4.0 |
| | 89-680 | 89-680 | CG | 1150 | 93.0 | - | R94 | 73 | 24 | 2 | 0 | 1 | 0 | Axial-[010] | 1.86 | 0.40 | 3.3371 | 4.1 | 3.4 | 2.4 | 1.8 |
| | L1 | L1A | VCG | - | - | - | - | 75 | 15 | 10 | 0 | 0 | 0 | Ortho | 21.3** | 0.49 | 3.3449 | 9.1 | 6.6 | 4.1 | 5.8 |
| | | L1B | VCG | - | - | - | - | 68 | 29 | 3 | 0 | 0 | 0 | Ortho | 4.27 | 0.74 | 3.3399 | 6.1 | 4.7 | 1.1 | 4.1 |
| | LS4 | LS4A | VCG | - | 92.4 | - | LCT01 | 78 | 14 | 3 | 5 | 0 | 0 | Ortho | 24.7** | 0.46 | 3.3700 | 10.0 | 7.2 | 4.5 | 6.3 |
| | | LS4B | VCG | - | - | - | - | 72 | 21 | 3 | 7 | 0 | 0 | Ortho | 13.7** | 0.48 | 3.3669 | 3.4 | 3.7 | 2.3 | 2.9 |
| | LS9 | LS9B | VCG | 1015 | 92.1 | 93.0 | This study | 73 (72) | 19 (19) | 8 (8) | 0 (0) | 0 (1) | 0 (0) | Axial-[010] | 4.57 | 0.32 | 3.3379 | 3.3 | 3.5 | 2.2 | 2.4 |
| | LS11 | LS11A | VCG | - | 92.3 | 92.9 | This study | 82 | 13 | 3 | 2 | 0 | 0 | Axial-[010] to ortho | 11.6** | 0.39 | 3.3569 | 10.1 | 6.7 | 4.3 | 5.1 |
| | | LS11B | VCG | - | - | - | - | 71 (70) | 24 (24) | 2 (2) | 3 (3) | 0 (1) | 0 (0) | Axial-[010] to ortho | 10.5** | 0.30 | 3.3563 | 6.8 | 6.2 | 4.7 | 3.8 |
| | LS15 | LS15 | G | - | 88.2 | - | LCT01 | 100 | 0 | 0 | 0 | 0 | 0 | Axial-[010] | 2.19 | 0.32 | 3.3550 | 8.1 | 4.9 | 4.0 | 2.1 |
| Olmani | 03-TZ-14E | 03-TZ-14E1 | CP | - | - | - | - | 68 | 32 | 0 | 0 | 0 | 0 | Axial-[100] to ortho | 6.00 | 0.80 | 3.3462 | 11.2 | 7.6 | 3.9 | 6.0 |
| | | 03-TZ-14E2 | CP | - | - | - | - | 89 | 10 | 0 | 0 | 0 | 0 | Axial-[100] to ortho | 7.41 | 0.67 | 3.6493 | 11.4 | 7.2 | 3.9 | 5.9 |
| | 03-TZ-14H | 03-TZ-14H | P | - | - | - | - | 90 | 9 | 1 | 0 | 0 | 0 | Axial-[100] | 5.31 | 0.86 | 3.3503 | 12.4 | 7.9 | 3.7 | 6.7 |
| | 03-TZ-14I | 03-TZ-14I | CP | - | - | - | - | 97 | 3 | 0 | 0 | 0 | 0 | Axial-[100] to ortho | 3.78 | 0.64 | 3.3540 | 11.1 | 8.2 | 5.3 | 5.4 |
| | 03-TZ-14J | 03-TZ-14J1 | CP | - | - | - | - | 99 | 1 | 0 | 0 | 0 | 0 | Axial-[100] to ortho | 43.2** | 0.66 | 3.3545 | 18.4 | 13.3 | 8.3 | 8.5 |
| | | 03-TZ-14J2 | CP | - | - | - | - | 100 | 0 | 0 | 0 | 0 | 0 | Axial-[100] to ortho | 44.5** | 0.66 | 3.3550 | 13.5 | 9.2 | 5.0 | 7.8 |
| | 03-TZ-14K | 03-TZ-14K | CG | - | 87.6 | 88.8 | This study | 43 | 53 | 4 | 0 | 0 | 0 | Axial-[100] to ortho | 1.81 | 0.45 | 3.3279 | 3.9 | 2.6 | 2.1 | 1.8 |
| | 03-TZ-14L | 03-TZ-14L | CG | - | - | - | - | 89 | 10 | 1 | 0 | 0 | 0 | Axial-[100] to ortho | 4.57 | 0.79 | 3.3498 | 11.7 | 7.8 | 3.8 | 6.3 |
| | 03-TZ-14M | 03-TZ-14M1 | CP | - | - | - | - | 82 | 18 | 0 | 0 | 0 | 0 | Axial-[100] | 5.59 | 0.79 | 3.3462 | 12.5 | 7.5 | 3.9 | 6.3 |
| | | 03-TZ-14M2 | CP | - | - | - | - | 84 | 16 | 0 | 0 | 0 | 0 | Axial-[100] | 5.75 | 0.71 | 3.3472 | 12.7 | 7.4 | 4.2 | 6.1 |
| | 03-TZ-14N | 03-TZ-14N1 | VCG | - | - | - | - | 100 | 0 | 0 | 0 | 0 | 0 | Ortho | 5.24 | 0.47 | 3.3547 | 10.2 | 7.7 | 5.5 | 4.3 |
| | | 03-TZ-14N2 | VCG | - | - | - | - | 100 | 0 | 0 | 0 | 0 | 0 | Ortho | 5.41 | 0.64 | 3.3550 | 10.1 | 6.5 | 4.2 | 4.5 |
| | OL3 | OL3A | CG | 1066 | 92.1 | 92.4 | This study | 44 | 53 | 3 | 0 | 0 | 0 | Axial-[100] | 1.87 | 0.88 | 3.3282 | 3.7 | 2.3 | 0.6 | 2.2 |
| | | OL3B | CG | - | - | - | - | 44 | 53 | 3 | 0 | 0 | 0 | Axial-[100] | 1.87 | 0.88 | 3.3282 | 3.7 | 2.3 | 0.6 | 2.1 |
| | OL10 | OL10 | VCG | - | 93.1 | - | LCT01 | 95 | 5 | 0 | 0 | 0 | 0 | Axial-[100] | 5.28 | 0.92 | 3.3525 | 11.6 | 7.3 | 3.4 | 6.2 |
| | OL-NN1 | OL-NN1 | P | - | - | - | - | 98 (97) | 2 (2) | 0 (0) | 0 (0) | 0 (1) | 0 (0) | Axial-[100] | 5.45 | 0.80 | 3.3485 | 13.8 | 9.8 | 5.0 | 7.1 |
| | OL-NN2 | OL-NN2 | CG | - | - | - | - | 98 (97) | 0 (0) | 2 (2) | 0 (0) | 0 (1) | 0 (0) | Axial-[100] to ortho | 4.00 | 0.59 | 3.3544 | 12.0 | 8.5 | 4.9 | 6.0 |
| | OL-NN3 | OL-NN3 | P | - | - | - | - | 97 | 0 | 3 | 0 | 0 | 0 | Axial-[100] to ortho | 8.95 | 0.72 | 3.3542 | 14.5 | 9.1 | 5.4 | 6.8 |
| | 89-772 | 89-772 | VCG | 950 | 87.6 | - | R94 | 98 | 0 | 2 | 0 | 0 | 0 | Axial-[010] | 3.11 | 0.30 | 3.3544 | 6.1 | 3.9 | 2.7 | 2.5 |
| | 89-773 | 89-773 | VCG | 1080 | 93.6 | - | R94 | 85 | 15 | 0 | 0 | 0 | 0 | Axial-[100] to ortho | 6.51 | 0.93 | 3.3471 | 12.5 | 7.8 | 3.8 | 6.4 |
| | 89-774 | 89-774 | VCG | - | 93.5 | - | R94 | 100 | 0 | 0 | 0 | 0 | 0 | Ortho | 8.08 | 0.48 | 3.3550 | 10.6 | 7.5 | 5.2 | 4.1 |
| | 89-776 | 89-776 | VCG | 1120 | 94.4 | - | R94 | 97 | 0 | 3 | 0 | 0 | 0 | Axial-[100] | 7.85 | 0.62 | 3.3544 | 11.8 | 8.2 | 3.8 | 6.4 |

* Modal compositions determined from EBSD maps. Values between parentheses give the modal contents including veins.
** Olivine J-index values overestimated because of the small number of grains indexed in very coarse-granular peridotites.
Reference for mg# and T data: R94= Rudnick et al. 1994; LCT01= Lee, 2001
CPO types: ortho= orthorhombic, axial-[100], axial-[010], axial-[100] to orthorhombic, and axial-[010] to orthorhombic crystal-preferred orientations, see main text for details.
J-indexes could not be calculated for samples in which less than 100 grains were measured.
Textures: G= granular; CG= Coarse-granular; VCG= Very coarse-granular; P= Porphyroclastic; CP= Coarse-porphyroclastic; M= Mylonitic

## 3. Methods

### 3.1 Pressure and temperature estimates

Major elements composition of olivine, orthopyroxene, clinopyroxene, garnet, and spinel were analyzed in 15 samples using a Cameca SX100 electron microprobe at Microsonde Sud facility, in Montpellier (France). Analytical conditions were a 20 kV accelerating voltage and a 10 nA probe current. Core and rim composition of 3 to 4 grains were measured for each mineral (mineral compositions of the analyzed samples presented in the online Supplementary Material Table 1).

When orthopyroxene and clinopyroxene were both present, the sample equilibrium temperature was calculated using the two pyroxenes Fe-Mg exchange geothermometer from Brey and Köhler (1990), which has an uncertainty of ±50°C. However, many of the samples are clinopyroxene-free harzburgites to dunites. To verify if other thermometers (Brey and Köhler, 1990; Fabriès, 1979; Li et al., 1995; Sachtleben and Seck, 1981; Wells, 1977; Witt-Eickschen and Seck, 1991) could be used to calculate the equilibrium temperatures for the clinopyroxene-free peridotites, the consistency between the temperatures calculated with the two pyroxenes geothermometer of Brey and Köhler (1990) and these thermometers was tested for the clinopyroxene-bearing peridotites. Because the discrepancies between the equilibrium temperatures obtained using different thermometers were large, we choose not to present temperatures calculated for the clinopyroxene-free samples. The equilibrium pressure was estimated in one garnet-bearing harzburgite from Lashaine (LS11) using the orthopyroxene-garnet barometer of Nickel and Green (1985), which has uncertainties of 0.2 GPa.

### 3.2 Electron-backscattered diffraction (EBSD)

The crystallographic preferred orientation (CPO) of olivine, pyroxenes, pargasite, phlogopite, spinel, and garnet was measured by indexation of electron back-scattered diffraction (EBSD) patterns at the SEM-EBSD facility, Geosciences Montpellier. These patterns are produced by interaction of a vertical incident electron beam and a carefully polished thin section tilted at 70° to the horizontal. Measurements were performed in a JEOL JSM 5600 scanning electron microscope using an acceleration voltage of 17 kV and a working distance of 23 mm. For each sample, maps covering nearly the entire thin section were obtained using steps between 100 and 30 μm, depending on grain size. Indexing rates varied between 60 to 90% depending of the mineral species and degree of fracturing present in the thin section. Phlogopite, when present, was usually poorly indexed. Orthopyroxene was sometimes misindexed as

clinopyroxene. Careful post-acquisition data treatment controlled by comparison between EBSD maps and microscopic observations was performed to reduce inaccurate mineral determination as well as misindexation due to olivine pseudosymmetry. Modal composition, grain sizes, and shape-preferred orientations were also obtained from the EBSD maps.

Crystal-preferred orientation data are displayed in pole figures, presented as lower hemisphere stereographic projections. Data were plotted as one point per grain to prevent over-representation of large grains. When the foliation and lineation could be identified, the orientation of the main crystallographic directions: [100], [010] and [001] for olivine and pyroxenes, was plotted relatively to the principal axes of the deformation ellipsoid X, Y, and Z. Because the foliation and lineation could not be identified in coarse-grained samples, thin sections were cut in random orientations. To make comparison between different samples easier, we rotated the CPO of randomly oriented samples into a common orientation in which the maximum concentration of olivine [100] and [010] axes are parallel to the E–W and the N–S directions of the pole figure, respectively.

To characterize the olivine CPO symmetry we computed the dimensionless BA index (where B and A stand for [010] and [100] axes, respectively, Mainprice et al., 2014) defined as:

$$BAindex = \frac{1}{2}\left(2 - \left(\frac{P010}{G010 + P010}\right) - \left(\frac{G100}{G100 + P100}\right)\right)$$

(1)

where P and G are the Point and Girdle fabric indices (Vollmer, 1990) of the olivine principal axes [100] and [010]. These indexes were calculated from the eigenvalues of the normalized orientation matrix, as $P=\lambda_1-\lambda_3$ and $G=2(\lambda_2-\lambda_3)$ using the MTEX texture analysis Matlab toolbox (Hielscher and Schaeben, 2008; Mainprice et al., 2011). The BA index allows a classification of the olivine CPO symmetry into 3 types: axial-[010] (BA index<0.35), orthorhombic (0.35<BA index<0.65), and axial-[100] (BA index>0.65).

The strength of the fabric was quantified using the dimensionless J-index, which is the volume-averaged integral of squared orientation densities:

$$J= f(g)2dg \qquad (2)$$

where f(g) is the orientation distribution function (ODF) and dg = dφ1dφdφ2 sinφπ2 (Bunge, 1982). φ1, φ, and φ2 are the Euler angles that define the rotations allowing for coincidence between the crystallographic and external reference frames. Olivine CPO in natural peridotites is characterized by J-indexes mostly between 2 and 20, with a peak at 8–10 (Ben Ismaïl and Mainprice, 1998; Tommasi et al., 2000). The J-index for each sample was

calculated based on the mean orientation of each grain using the MTEX texture analysis Matlab toolbox (Hielscher and Schaeben, 2008).

## 3.3 Seismic properties

Seismic properties of Tanzanian xenoliths were calculated using the CPO of all major phases and their respective modal content estimated from EBSD maps (Mainprice, 1990). For olivine, orthopyroxene, clinopyroxene, garnet, amphibole, and phlogopite single-crystal elastic constant tensors at ambient conditions were used (Abramson et al., 1997; Bezacier et al., 2010; Chai et al., 1997a, Chai et al., 1997b, Collins and Brown, 1998). A Voigt-Reuss-Hill averaging was applied in all calculations. The seismic anisotropy parameters and the elastic constants of all samples are presented in Table 1 and online Supplementary Material 2, respectively.

Average seismic properties were also calculated for Lashaine, Olmani, and rift axis localities by averaging the individual samples elastic constant tensors for each locality. This calculation results in a maximum estimation of the seismic anisotropy for the locality, as it relies on the assumption of a common orientation of the foliation and lineation for all samples.

## 3.4 Fourier transform infrared spectroscopy (FTIR)

Fifteen double-polished thin sections were prepared for unpolarized FTIR analysis. Before analysis, the sections were immersed in pure acetone for at least 12h to dissolve any intergranular CrystalBond glue. FTIR spectroscopy analyses were performed at the Laboratoire des Colloïdes, Verres, Nanomatériaux at Montpellier University using a Bruker IFS66v coupled with a Bruker HYPERION microscope and mercury-cadmium-telluride (MCT) detector cooled by liquid nitrogen. A Globar light source and a Ge-KBr beam splitter were used to generate unpolarized mid-infrared radiation. A background measurement was performed at the beginning of the analysis of each sample and repeated when necessary. Measurements were made on olivine, orthopyroxene, and garnet crystals using a square aperture 30 to 100 μm wide. No measurement could be made on clinopyroxene crystals, which were too small and too altered. Two hundred scans were accumulated with a resolution of 4 cm− 1 for each measurement. A baseline correction was applied on each spectrum using the OPUS software. Spectra were then normalized to a sample thickness of 1 cm. The sample thickness was measured using a micrometer with a tolerance of ± 1 μm, and was always near 500 μm (Table 2). Fractures and inclusions were strictly avoided.

Table 2: Mineral OH concentrations derived from FTIR analyses.

| Locality | Sample | Temperature (°C) | Ol Mg # | Reference for mg# and T data | Texture | Texture complement | Olivine CPO | Mineral | Section thickness (µm) | Paterson calibration[a] OH concentrations ($H/10^6$ Si) | OH concentrations (ppm wt $H_2O$) | Average OH concentrations (ppm wt $H_2O$) | Olivine - Withers calibration[b] OH concentrations (ppm wt $H_2O$) | Average OH concentrations (ppm wt $H_2O$) |
|---|---|---|---|---|---|---|---|---|---|---|---|---|---|---|
| **Eledoi** | EL6 | - | 90.3 | LCT01 | Granular | Vein-bearing | Axial-[100] to ortho | ol-4 | 538 | 114 | 7 | **9** | 13 | **15** |
| | | | | | | | | ol-8 | 538 | 160 | 10 | | 18 | |
| | | | | | | | | ol-12 | 538 | 151 | 9 | | 17 | |
| | | | | | | | | ol-13 | 538 | 192 | 12 | | 21 | |
| | | | | | | | | ol-14 | 538 | 74 | 5 | | 8 | |
| | EL15a | 1052 | 90.1 | This study | Granular | Vein-bearing | Axial-[100] | ol-1 | 541 | 65 | 4 | **8** | 7 | **14** |
| | | | | | | | | ol-2 | 541 | 103 | 6 | | 11 | |
| | | | | | | | | ol-5 | 541 | 126 | 8 | | 14 | |
| | | | | | | | | ol-11 | 541 | 185 | 11 | | 20 | |
| | | | | | | | | ol-12 | 541 | 178 | 11 | | 20 | |
| | | | | | | | | opx-2 | 541 | 2204 | 198 | **209** | - | - |
| | | | | | | | | opx-3 | 541 | 2507 | 225 | | - | |
| | | | | | | | | opx-4 | 541 | 1657 | 149 | | - | |
| | | | | | | | | opx-5 | 541 | 2031 | 182 | | - | |
| | | | | | | | | opx-9 | 541 | 2121 | 190 | | - | |
| | | | | | | | | opx-10 | 541 | 3427 | 308 | | - | |
| | EL15b | 1052 | 90.1 | This study | Granular | Vein-bearing | Axial-[100] | ol-2 | 527 | 70 | 4 | **4** | 8 | **7** |
| | | | | | | | | ol-3 | 527 | 48 | 3 | | 5 | |
| | | | | | | | | ol-4 | 527 | 56 | 3 | | 6 | |
| | | | | | | | | ol-5 | 527 | 49 | 3 | | 5 | |
| | | | | | | | | ol-7 | 527 | 46 | 3 | | 5 | |
| | | | | | | | | ol-10 | 527 | 49 | 3 | | 5 | |
| | | | | | | | | ol-11 | 527 | 109 | 7 | | 12 | |
| | | | | | | | | opx-1 | 527 | 2482 | 223 | **186** | - | - |
| | | | | | | | | opx-3 | 527 | 1902 | 171 | | - | |
| | | | | | | | | opx-4 | 527 | 1862 | 167 | | - | |
| | | | | | | | | opx-7 | 527 | 2043 | 183 | | - | |
| **Pello Hill** | PEL7 | - | 92.3 | LCT01 | Porphyroclastic | - | Ortho | ol-5 | 528 | 99 | 6 | **6** | 11 | **11** |
| | | | | | | | | ol-8 | 528 | 78 | 5 | | 9 | |
| | | | | | | | | ol-9 | 528 | 160 | 10 | | 18 | |
| | | | | | | | | ol-10 | 528 | 43 | 3 | | 5 | |
| | | | | | | | | opx-2 | 528 | 1538 | 138 | **133** | - | - |
| | | | | | | | | opx-3 | 528 | 1419 | 127 | | - | |
| | PEL15 | - | 92.4 | LCT01 | Mylonitic | - | Ortho | ol-2 | 496 | 77 | 5 | **3** | 8 | **5** |
| | | | | | | | | ol-5 | 496 | 28 | 2 | | 3 | |
| | | | | | | | | ol-8 | 496 | 32 | 2 | | 4 | |
| | | | | | | | | opx-1 | 496 | 1727 | 155 | **212** | - | - |
| | | | | | | | | opx-2 | 496 | 2764 | 248 | | - | |
| | | | | | | | | opx-3 | 496 | 1930 | 173 | | - | |
| | | | | | | | | opx-4 | 496 | 2488 | 223 | | - | |
| | | | | | | | | opx-5 | 496 | 2561 | 230 | | - | |
| | | | | | | | | opx-6 | 496 | 2789 | 250 | | - | |
| | | | | | | | | opx-7 | 496 | 2416 | 217 | | - | |
| | | | | | | | | opx-8 | 496 | 2233 | 201 | | - | |
| | | | | | | | | opx-10 | 496 | 2313 | 208 | | - | |

Table 2 (suite)

| Locality | Sample | Temperature (°C) | Ol Mg # | Reference for mg# and T data | Texture | Texture complement | Olivine CPO | Mineral | Section thickness (µm) | Paterson calibration[a] | | | Olivine - Withers calibration[b] | |
|---|---|---|---|---|---|---|---|---|---|---|---|---|---|---|
| | | | | | | | | | | OH concentrations (H/$10^6$ Si) | OH concentrations (ppm wt $H_2O$) | Average OH concentrations (ppm wt $H_2O$) | OH concentrations (ppm wt $H_2O$) | Average OH concentrations (ppm wt $H_2O$) |
| | PEL16 | - | 92.5 | This study | Porphyroclastic | - | Axial-[100] to ortho | ol-2 | 506 | 46 | 3 | **4** | 5 | **7** |
| | | | | | | | | ol-4 | 506 | 59 | 4 | | 6 | |
| | | | | | | | | ol-5 | 506 | 51 | 3 | | 6 | |
| | | | | | | | | ol-7 | 506 | 78 | 5 | | 9 | |
| | | | | | | | | ol-8 | 506 | 91 | 6 | | 10 | |
| | PEL17 | - | 92.4 | This study | Mylonitic | - | Axial-[100] | ol-2 | 543 | 24 | 1 | **2** | 3 | **4** |
| | | | | | | | | ol-3 | 543 | 49 | 2 | | 5 | |
| | | | | | | | | opx-1 | 543 | 1053 | 65 | **97** | - | - |
| | | | | | | | | opx-2 | 543 | 1632 | 100 | | - | |
| | | | | | | | | opx-4 | 543 | 2739 | 168 | | - | |
| | | | | | | | | opx-6 | 543 | 1268 | 78 | | - | |
| | | | | | | | | opx-7 | 543 | 1231 | 75 | | - | |
| | PEL34 | - | - | LCT01 | Porphyroclastic | - | Axial-[100] | ol-1 | 537 | 46 | 3 | **3** | - | - |
| | | | | | | | | ol-2 | 537 | 33 | 2 | | - | |
| | | | | | | | | ol-3 | 537 | 63 | 4 | | - | |
| | | | | | | | | ol-5 | 537 | 36 | 2 | | - | |
| | | | | | | | | ol-6 | 537 | 48 | 3 | | - | |
| | | | | | | | | ol-7 | 537 | 50 | 3 | | - | |
| | | | | | | | | ol-8 | 537 | 42 | 3 | | - | |
| | | | | | | | | ol-9 | 537 | 57 | 4 | | - | |
| | PEL39 | - | 90.1 | LCT01 | Granular | - | Axial-[100] | ol-5 | 476 | 28 | 2 | **3** | 3 | **5** |
| | | | | | | | | ol-6 | 476 | 46 | 3 | | 5 | |
| | | | | | | | | ol-9 | 476 | 49 | 3 | | 5 | |
| | | | | | | | | ol-10 | 476 | 67 | 4 | | 7 | |
| | PEL40 | - | 91.0 | LCT01 | Porphyroclastic | vein-bearing | Ortho | ol-1 | 567 | 52 | 3 | **5** | 6 | **10** |
| | | | | | | | | ol-2 | 567 | 131 | 8 | | 14 | |
| | | | | | | | | ol-4 | 567 | 79 | 5 | | 9 | |
| | PEL41 | - | 87.9 | LCT01 | Coarse-granular | vein-bearing | Axial-[100] | ol-1 | 499 | 216 | 13 | **12** | 24 | **21** |
| | | | | | | | | ol-2 | 499 | 259 | 16 | | 29 | |
| | | | | | | | | ol-3 | 499 | 288 | 18 | | 32 | |
| | | | | | | | | ol-4 | 521 | 171 | 10 | | 19 | |
| | | | | | | | | ol-5 | 521 | 182 | 11 | | 20 | |
| | | | | | | | | ol-6 | 521 | 158 | 10 | | 17 | |
| | | | | | | | | ol-7 | 499 | 239 | 15 | | 26 | |
| | | | | | | | | ol-9 | 499 | 45 | 3 | | 5 | |
| | | | | | | | | ol-10 | 521 | 179 | 11 | | 20 | |
| **Olmani** | 89-772 | 950 | 87.6 | R94 | Very coarse-granular | - | Axial-[010] | ol-2 | 528 | 86 | 5 | **5** | 9 | **10** |
| | OL10 | - | 93.1 | LCT01 | Very coarse-granular | - | Axial-[100] | ol-1 | 564 | 50 | 3 | **3** | 6 | **6** |
| | | | | | | | | ol-2 | 564 | 75 | 5 | | 8 | |
| | | | | | | | | ol-3 | 564 | 50 | 3 | | 6 | |
| | | | | | | | | ol-4 | 564 | 51 | 3 | | 6 | |
| | | | | | | | | ol-8 | 564 | 43 | 3 | | 5 | |
| | 03TZ14J | - | - | - | Coarse porphyroclastic | - | Axial-[100] to ortho | ol-1 | 500 | 85 | 5 | **4** | 9 | - |
| | | | | | | | | ol-2 | 500 | 75 | 5 | | 8 | |
| | | | | | | | | ol-3 | 500 | 72 | 4 | | - | |
| | | | | | | | | ol-5 | 500 | 57 | 3 | | - | |
| | | | | | | | | ol-6 | 500 | 85 | 5 | | - | |
| **Lashaine** | LS11 | - | 92.3 | This study | Very coarse-granular | - | Axial-[010] to ortho | ol-1 | 491 | 203 | 12 | **12** | 22 | **21** |
| | | | | | | | | ol-2 | 491 | 215 | 13 | | 24 | |
| | | | | | | | | ol-3 | 491 | 204 | 13 | | 22 | |
| | | | | | | | | ol-4 | 491 | 196 | 12 | | 22 | |
| | | | | | | | | ol-5 | 491 | 154 | 9 | | 17 | |
| | | | | | | | | opx-2 | 491 | 1133 | 98 | **121** | - | - |
| | | | | | | | | opx-3 | 491 | 1648 | 143 | | - | |

[a] OH concentrations from this study calculated using the calibration of Paterson (1982) have ±30% error (Kohlstedt et al., 1996); [b] OH concentrations corrected by a factor of 1.8 according to Withers et al. (2012).
Reference for mg# and T data: R94= Rudnick et al., 1994; LCT01= Lee, 2001.

CPO types: Ortho= orthorhombic, axial-[100], axial-[010], axial-[100] to orthorhombic, and axial-[010] to orthorhombic crystal-preferred orientations, see text for details.

The calibration of Paterson (1982) was used to quantify the OH concentration:

$$C_{OH} = \frac{X_i}{150\zeta} \int \frac{k(\bar{v})}{(3780 - \bar{v})} d\bar{v}$$

(3)

where $C_{OH}$ is the hydroxyl concentration (in mol H/l), $\zeta$ is an orientation factor (1/3 for unpolarized measurements), and $k(\bar{v})$ is the absorption coefficient in cm$^{-1}$ for a given wavenumber $\bar{v}$. $X_i$ is a density factor, which depends on the mineral phase ($X_{i(ol,\ Fo90)}$ = 2695 wt. ppm $H_2O$, $X_{i(orthopyroxene)}$ = 2812 wt. ppm $H_2O$). The uncertainty in the resulting OH concentrations are ~30% (Kohlstedt et al., 1996).

We also converted the olivine OH concentrations (See Table 2) obtained using the calibration of Paterson (1982) to the new calibration of Withers et al. (2012). The conversion factor between the two calibrations is a function of the sample thickness and of the OH concentration obtained with the calibration of Paterson (1982). Here, the sample thickness is comprised between 476 and 567 μm and the olivine OH concentrations range between 1 and 18 wt. ppm $H_2O$. Therefore, the olivine OH concentrations must be multiplied by a factor of 1.8 (see Withers et al., 2012, Supplementary material Figure 1).
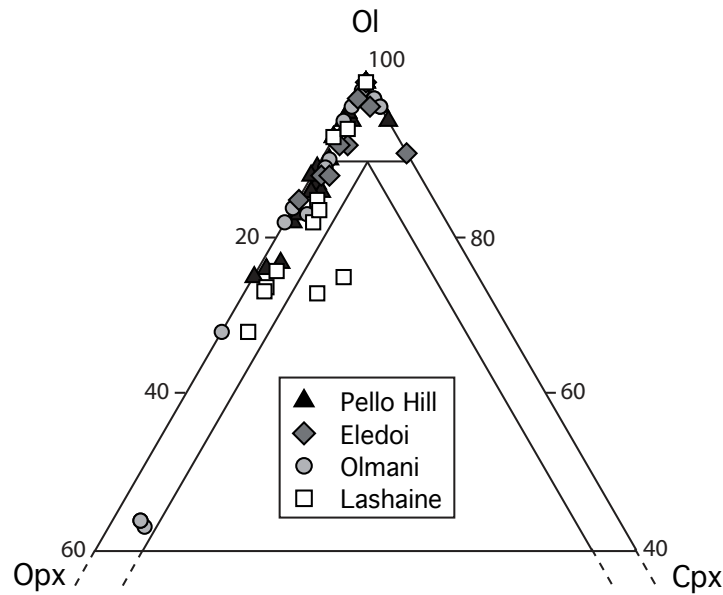


Figure 2: Olivine-orthopyroxene-clinopyroxene modal ratios in the studied peridotites studied here. Modal compositions are derived from EBSD maps, not considering metasomatic veins and pockets, and recalculated for a total of 100% of olivine+orthopyroxene+clinopyroxene.

# 4. Results

## 4.1 Compositions and equilibrium conditions

All samples are garnet-free peridotites, except for four Lashaine peridotites (LS11, LS4, L1, and 89-680). Most samples have harzburgitic to dunitic compositions (Fig. 2 and Table 1). Orthopyroxene contents vary mainly between 0 and 20%, but several samples from Lashaine, Olmani and Pello Hill display higher modal orthopyroxene contents (22 to 32%) and two samples from Olmani have >50% orthopyroxene (OL3 and 03TZ14K). Secondary minerals present in diffuse veins or pockets include clinopyroxene, amphibole, phlogopite, and spinel. Veins may comprise up to 15% of the total rock (modal contents including the veins are given in parentheses in Table 1).

Mineral compositions are presented in the online Supplementary Material Table 1. In most samples, olivine has a high Mg# (Mg#: atomic Mg/(Fe+Mg)), which varies between 90.1 and 94.4 (Table 1). Seven samples (out of the forty-one for which the olivine Mg# has been measured) have more Fe-rich olivines (Fo ≤ 89). Among these samples, 4 are very-coarse granular dunites from Olmani or from the rift axis localities (EL14, PEL11, PEL41, 89-772). The 3 other Fe-rich samples are: a harzburgite from Olmani with high orthopyroxene contents (>50%; 03TZ14K), a granular dunite from Lashaine (LS15), and a porphyroclastic harzburgite from Pello Hill (PEL1). There is no significant difference between olivine Mg# for samples from the in-axis and off-axis localities. Olivine always has NiO > 0.25 wt.% and low CaO (≤ 0.11 wt.%). Orthopyroxenes are enstatite, with Mg# > 90. Clinopyroxenes are Cr-bearing diopside ($Cr_2O_3$ comprised between 1.0 and 3.7 wt.%) with Mg# > 90, except for sample EL15 where $Cr_2O_3$ < 0.1 wt.% and lower Mg# are measured. Spinels have high MgO (10-17 wt%) and variable Cr# (atomic Cr/(Cr+Al)), ranging between 36 and 89.

We have been able to estimate equilibrium temperatures for only 9 of the 15 samples analyzed, because the others lacked clinopyroxene. Independently of their provenance or microstructure, all these samples have core equilibrium temperatures (calculated from core compositions in orthopyroxene and clinopyroxene) between 1000 and 1100°C ±50°C (Table 1). Rim equilibrium temperatures (calculated from rim compositions in orthopyroxene and clinopyroxene) tend to be slightly, but systematically lower (by 5-21°C), except for sample PEL22 from Pello Hill, where rim equilibrium temperature is lower than core equilibrium temperature by >100°C (960°C versus 1090°C). In a garnet harzburgite from Lashaine (LS11), rim and core equilibrium pressures of 3.3 GPa and 3.1 GPa were obtained, respectively.
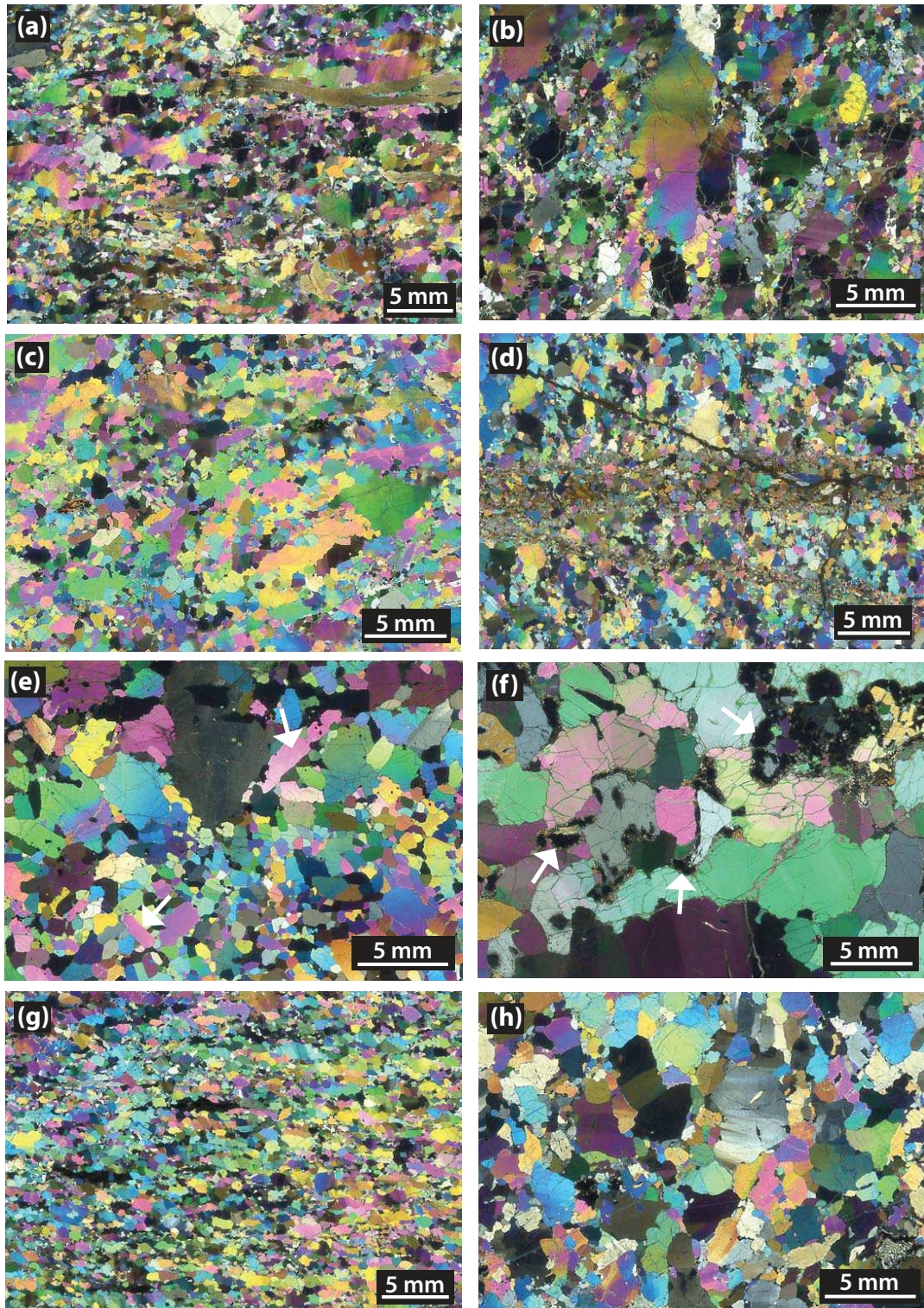
Figure 3: Photomicrographs in cross-polarized light showing typical microstructures for the studied xenoliths. (a) Mylonite PEL17B, showing highly elongated orthopyroxenes and olivines, with strong intracrystalline deformation (undulose extinction, subgrains, kinks) surrounded by a finer-grained matrix composed mainly of olivine. (b) Porphyroclastic peridotite PEL7, with large olivine porphyroclasts displaying closely-spaced subgrain boundaries, surrounded by small polygonal olivine neoblasts. (c) Porphyroclastic peridotite PEL1, showing large olivine porphyroclasts with widely-spaced subgrains and polygonal neoblasts devoid of

substructure. (d) Porphyroclastic peridotite EL15, displaying olivine grains with well-defined subgrain boundaries, as well as diffuse metasomatic veins that crosscut the foliation. (e) Coarse-granular dunite PEL11 showing large olivine grains with rare subgrains, frequent polygonal grain boundaries and triple junctions and, locally, subautomorphic olivine crystals devoid of any substructure (marked by arrows). (f) Very coarse-grained peridotite LS4A from Lashaine, showing large olivine grains with curvilinear boundaries and widely spaced subgrain boundaries and orthopyroxenes rimmed by garnet (arrows). (g) Porphyroclastic peridotite OL-NN4 from Olmani showing elongated olivine porphyroclasts with well-defined subgrain boundaries. (h) Very coarse-grained harzburgite 89-773 from Olmani, showing large olivines with curvilinear boundaries.

## 4.2 Microstructures

Because of their very different characteristics, the xenoliths microstructures will be described as a function of their provenance: the rift axis (Pello Hill and Eledoi) or the transverse volcanic belt (Lashaine and Olmani).

### 4.2.1 Rift axis samples

The xenoliths from volcanic localities within the rift axis display variable microstructures. Among the 27 studied xenoliths, 2 are mylonitic, 22 are porphyroclastic, and 3 are coarse-granular to tabular.

*Mylonitic microstructures* are only observed in 2 samples from Pello Hill (PEL15 and PEL17; Fig. 3a). These rocks are characterized by centimeter-sized orthopyroxenes, which are highly elongated (aspect ratios of up to 15:1), defining the lineation. These orthopyroxenes always display well-defined kink bands and undulose extinctions. They have indented grain boundaries, with olivine grains filling the embayments or even forming vein-like inclusions parallel to the orthopyroxene elongation (Fig. 4a). Exsolution in orthopyroxene is ubiquitous. Olivine is present as plurimillimetric porphyroclasts and as recrystallized grains with sizes ranging from 0.4 to 2 mm. It displays curvilinear boundaries, evolving sometimes to polygonal shapes. Subgrain boundaries in olivine are highly oblique to perpendicular to the grains elongation. The frequency and extent of deformation features in the porphyroclasts vary, however, between the 2 samples. In mylonite PEL17, subgrain boundaries are well developed and closely spaced. In mylonite PEL15, there are fewer subgrain boundaries. In both mylonites, the olivine neoblasts exhibit few subgrain boundaries and sometimes form 120° triple junctions.
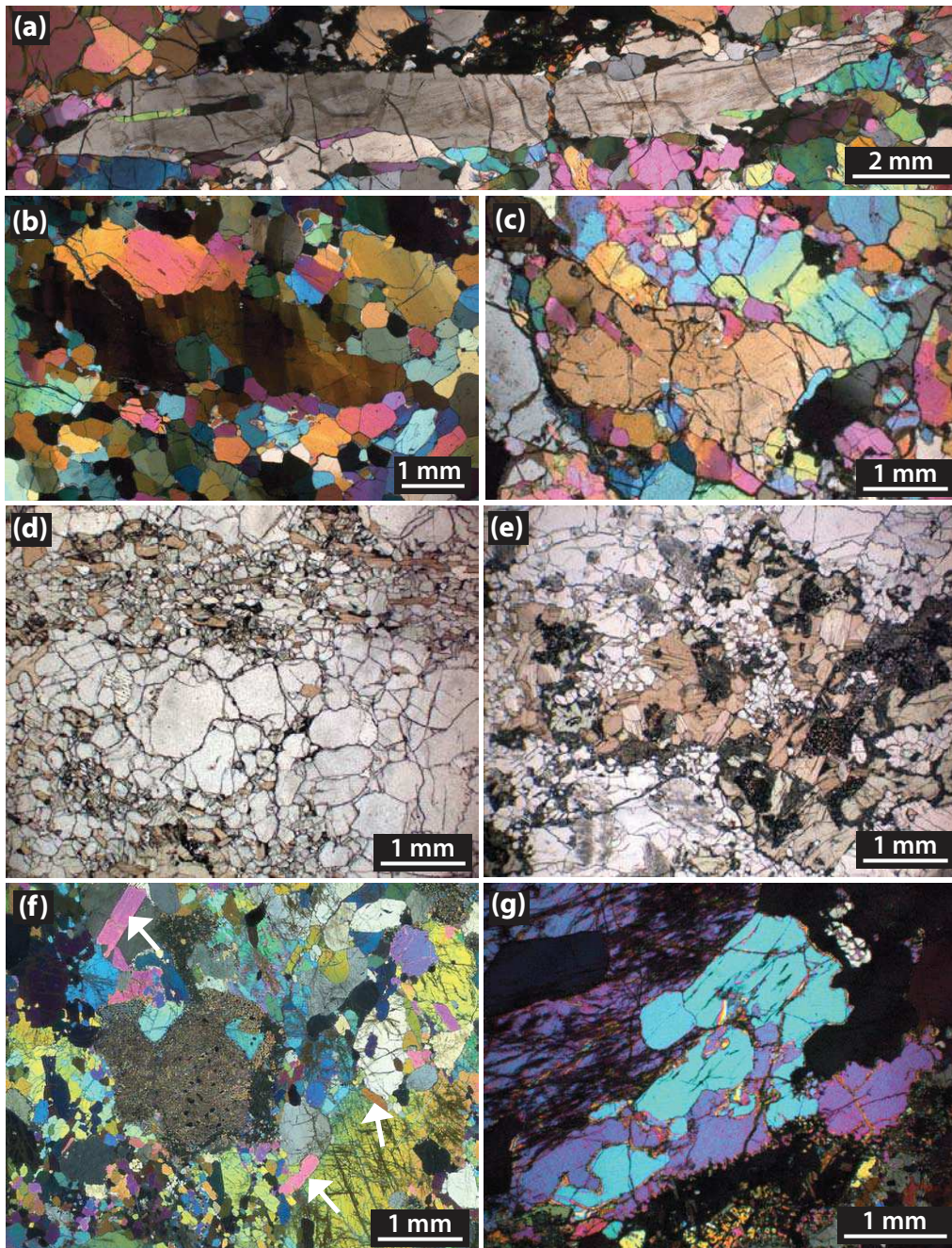
Figure 4: Photomicrographs in cross-polarized (a, b, c, f, and g) and plane-polarized light (d and e) of: (a) Highly elongated orthopyroxene in mylonite PEL15 from Pello Hill displaying embayments filled with olivine in crystalline continuity with the surrounding grains, as well as olivine inclusions elongated parallel to the orthopyroxene elongation and displaying subgrains. (b) Elongated olivine porphyroclasts with closely-spaced subgrain boundaries in peridotite PEL1 from Pello Hill. Small neoblasts forming triple junctions are also visible. (c) Orthopyroxene displaying inclusions and embayments filled with olivine in peridotite PEL7 from Pello Hill. (d) Diffuse veins composed of clinopyroxene, phlogopite, amphibole, spinel, and olivine in peridotite PEL39 from Pello Hill. The same phases are also present as interstitial grains between the veins. (e) Phlogopite, amphibole, clinopyroxene, and spinel "pockets" in peridotite PEL12 from Pello Hill. Note the smaller grain size and more polygonal shapes of olivine within these metasomatic pockets and veins. (f) Peridotite LS9 from Lashaine, characterized by coexistence of large olivine grains and of "recrystallized" zones composed of small

olivine neoblasts with polygonal shapes. Olivine tablets (arrows) growing on other grains are also visible. (g) Interpenetrating olivine-olivine grain boundaries, indicating active grain boundary migration in peridotite LS9 from Lashaine.

The *porphyroclastic peridotites* (Fig. 3b, c) are the most common textural type at Pello Hill; though less common, they are also present at Eledoi. They display plurimillimetric elongated olivine porphyroclasts (Fig. 3b), with common subgrain boundaries, undulose extinction, and sutured grain boundaries. Subgrain boundaries in olivine are dominantly at high angle to the foliation, but in many grains 2 orthogonal subgrain boundary families are observed (Fig. 4b). Small olivine neoblasts have fewer intracrystalline deformation features and tend to have more polygonal shapes, sometimes forming triple junctions. The frequency of the triple junctions in the recrystallized matrix and the subgrain boundaries spacing in porphyroclasts varies from sample to sample. For example, in sample PEL7, olivine porphyroclasts exhibit closely spaced subgrain boundaries and serrated grain boundaries (Fig. 4b), whereas olivine porphyroclasts in sample PEL1 display fewer subgrain boundaries and have polygonal grain boundaries (Fig. 3c). In the porphyroclastic peridotites from Eledoi, olivine porphyroclasts are rare, giving to the rock a more homogeneous microstructure. Interpenetrating olivine-olivine grain boundaries are common (Figs. 3b,c), suggesting grain boundary migration. In both sites, when present, orthopyroxene is anhedral, with intracrystalline deformation features, such as kink bands and undulose extinction. Exsolutions and corrosion embayments filled with olivine are common (Figs. 3b and 4c).

All *coarse-granular* to *tabular peridotites* are dunites (Fig. 3d,e). They exhibit coarse olivine grains (1-8 mm) with equant to tabular shapes. Olivine has curvilinear to polygonal boundaries and is often devoid of any substructure. 120° triple junctions are common. Six coarse-granular to tabular dunites (EL6, EL14, EL15, PEL39, PEL40 and PEL41) are crosscut by diffuse veins composed of millimeter-sized clinopyroxene, phlogopite, amphibole and spinel (Fig. 3d, 4d). Intracrystalline deformation features are very rarely observed in phlogopite and amphibole grains. The orthopyroxene crystals in contact with the vein are partially replaced by diopside.

In the porphyroclastic and mylonitic samples, the distribution of metasomatic minerals (phlogopite, amphibole, clinopyroxene, and spinel) is usually more diffuse. They form irregular pockets (Fig. 4e) or occur as small interstitial grains dispersed in the rock. When these minerals are dispersed in the rock, they may display subgrain boundaries. They are

usually associated with fine-grained olivines, forming "bands" with smaller grain sizes. In the pockets, spinel grows on clinopyroxene, pargasite or phlogopite (Fig. 4e).

### *4.2.2 Xenoliths from the transverse volcanic belt*

The xenoliths from the two localities (Olmani and Lashaine) within the divergence exhibit different microstructures. We will thus describe them separately.

### *4.2.2.1 Lashaine*

The xenoliths from Lashaine show mainly very coarse granular microstructures (Fig. 3f). Olivine grain size ranges from few millimeters to more than a centimeter. They have curvilinear boundaries and widely spaced subgrain boundaries. Interpenetrating grain boundaries are common. Orthopyroxene is usually smaller (1-8 mm) than olivine, with rare kink bands or undulose extinction. Exsolution in orthopyroxene is only observed in sample LS4. Lashaine is the only location where garnet peridotites (samples LS4, LS11, 89-680, and L1) were sampled. Garnet is present as irregularly-shaped crystals, several mm long, most often rimming orthopyroxene (marked by arrows in Fig. 3f). Kelyphitic rims are always present. In sample L1, garnet has been entirely replaced by kelyphite. Clinopyroxene is present as exsolutions in orthopyroxene or as very small interstitial crystals associated with pargasite and spinel. Olivine with interpenetrating boundaries is commonly observed (Figs. 3f and 4g), as well as orthopyroxene embayments filled with olivine. Peridotite LS9 displays slightly different characteristics: it contains recrystallized zones with finer-grained olivine showing curvilinear to polygonal boundaries (Fig. 4f). Olivine tablets free of any substructure form on other olivine crystals (Fig. 4f). Orthopyroxene often contains olivine inclusions.

Two samples have granular microstructures but smaller grain sizes: the coarse-granular harzburgite 89-680 and the granular dunite LS15. In harzburgite 89-680, olivine grain size ranges mainly between 1 and 4 mm. Olivine displays curvilinear to polygonal boundaries, and few subgrain boundaries. Orthopyroxene grain size varies between 0.5 and 2 mm. It has irregular shapes with curvilinear boundaries and may contain kink bands. Small interstitial clinopyroxene, phlogopite and amphibole grains are present. Dunite LS15 displays even smaller olivine grain sizes, ranging between 0.5 and 2 mm. Olivine has curvilinear, sometimes interpenetrating grain boundaries and a higher proportion of subgrain boundaries than the other samples from Lashaine.

*4.2.2.2 Olmani*

The peridotites from Olmani display microstructures intermediate between those described for peridotites from the rift-axis localities and from Lashaine. Among the 18 studied xenoliths, 5 are porphyroclastic, 4 are coarse-porphyroclastic, 4 are coarse-granular, and 5 are very coarse -granular.

The *porphyroclastic harzburgites* display elongated olivine porphyroclasts with millimetric grain sizes (Fig. 3g), which mark the foliation, and small olivine neoblasts (0.2-1 mm) with curvilinear to polygonal boundaries. The frequency of subgrain boundaries and the degree of polygonization of the grain boundaries vary from sample to sample. For instance, sample 03TZ14H shows interpenetrating olivine-olivine grain boundaries, whereas polygonal olivine grains characterize sample OL-NN4. Orthopyroxene occurs as small (<1mm), interstitial crystals displaying rare kink bands.

In *coarse-porphyroclastic harzburgites*, olivine grains are millimetric to centimetric and elongated. They commonly display closely spaced subgrain boundaries and interpenetrating grain boundaries. Small olivine grains rim the porphyroclasts. These neoblasts display curvilinear to polygonal grain boundaries. Orthopyroxene usually display irregular shapes, rare kink bands, and undulose extinction, as well as common exsolutions and corrosion embayments filled with olivine. Olivine crystals included in orthopyroxene grains are sometimes observed. In sample 03TZ14M, spinel-pyroxene symplectites are observed.

In *coarse-granular harzburgites*, olivine and orthopyroxene grain size varies between 0.5 and 3 mm. Two of these samples (OL3 and 03TZ14K) display very high orthopyroxene content (>50%). Olivine is characterized by curvilinear to polygonal boundaries and common subgrain boundaries. In 2 samples (03TZ14K and 03TZ14L), olivine is occasionally included in orthopyroxene. Orthopyroxene grains are anhedral. They display well-defined kink bands and undulose extinction, as well as exsolutions. In several orthopyroxene grains, corrosion embayments filled with olivine are present.

The *very coarse-granular peridotites* from Olmani are similar to the samples from Lashaine (Fig. 3h). They display millimetric to centimetric olivine grains. The density of subgrain boundaries and their spacing vary considerably from one sample to another. Interpenetrating olivine grain boundaries are always observed. Orthopyroxene is present in only 1 of these samples (89-773). In this sample, orthopyroxene has millimeter grain sizes, curvilinear boundaries, and displays well-defined kink bands.

## 4.3 Crystallographic preferred orientations (CPO)

As for the microstructures, we describe separately the CPOs of peridotites from the rift axis, Lashaine, and Olmani
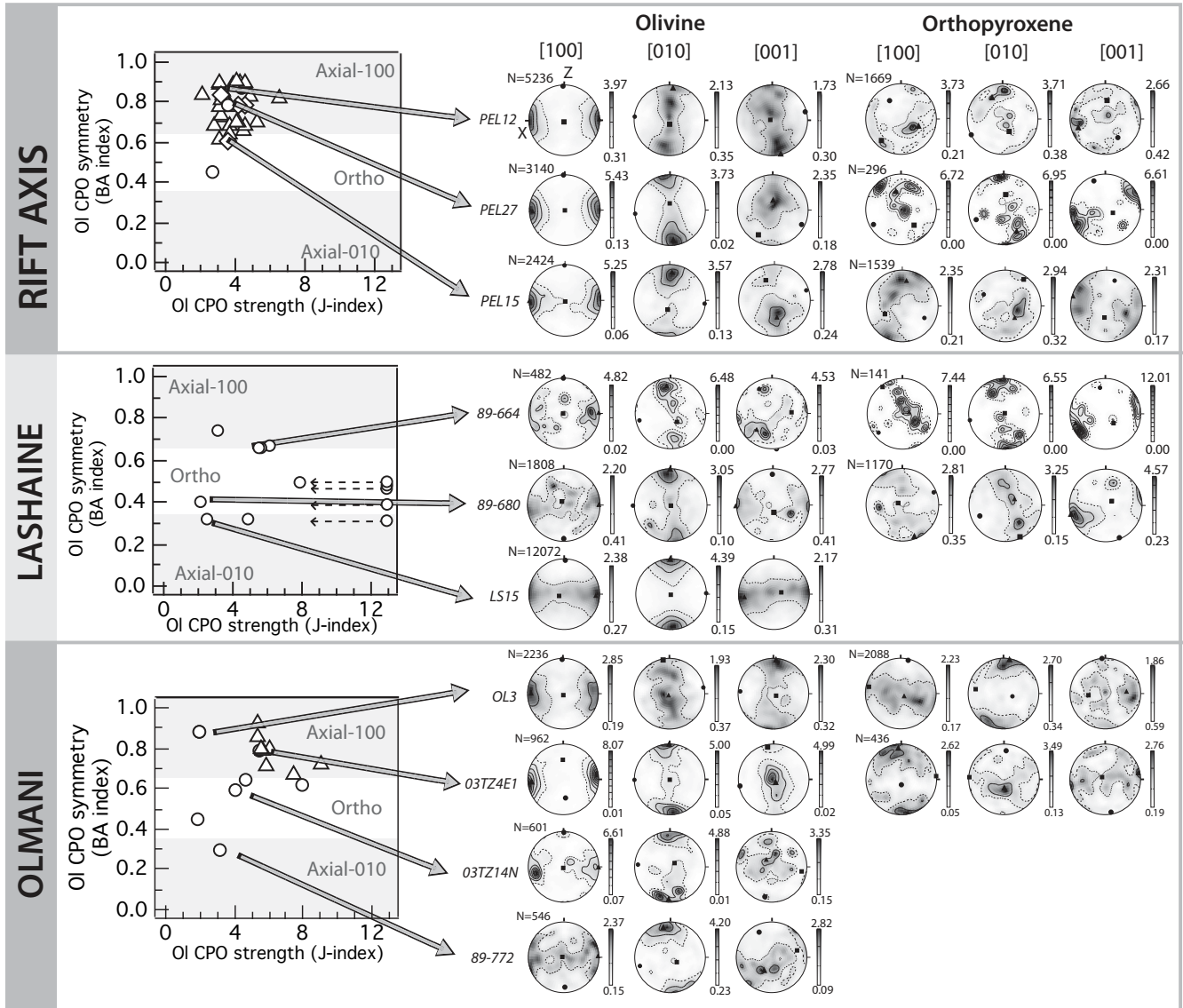


Figure 5: Olivine and orthopyroxene crystal preferred orientations (CPO): Olivine CPO strength (J-index) vs. symmetry (BA index) for all samples (granular, porphyroclastic and mylonitic microstructures symbolized by circles, squares, and diamonds, respectively) and pole figures of selected representative samples from the rift axis, Lashaine, and Olmani localities. Contours at 1 multiple of a uniform distribution. Dashed arrows indicate the samples in Lashaine where olivine J-index is overestimated because of the small number of indexed grains in coarse-grained peridotites.

## 4.3.1 Rift axis

Most rift-axis samples have low olivine CPO strength, with J-indexes varying mainly between 2-6 (Fig. 5). There is no correlation between the olivine CPO symmetry, its strength, and the microstructure. Peridotites from Pello Hill and Eledoi exhibit olivine CPO symmetries ranging from axial-[100] to orthorhombic (Fig. 5). Axial-[100] symmetry predominates. These patterns are characterized by a point concentration of [100], which in the mylonites and porphyroclastic peridotites is close to the lineation, and a girdle distribution of [010] and [001] normal to it. One sample has a clear orthorhombic olivine CPO, exhibiting a point concentration of the 3 crystallographic axes, with [100] showing the strongest concentration subparallel to the lineation. [010] is usually more concentrated than [001] and tends to align normal to the foliation. Most samples, like PEL27, display an intermediate pattern characterized by weak girdles of [010] and [001] normal to the maximum concentration of [100], with a concentration of [010] normal to the foliation plane and a concentration of [001] in the foliation plane parallel to the Y structural axis.

When present, orthopyroxene has more dispersed CPO, but correlated to the olivine CPO: the maximum concentration of [001] of orthopyroxene is parallel or slightly oblique to the olivine [100] maximum, except for one sample (PEL22). Orthorhombic CPO predominates, with [001] showing the strongest point concentration, which, in the mylonites and porphyroclastic peridotites, is subparallel to the lineation. In most samples, [100] axes are aligned normal to the foliation, but in some samples [010] is preferentially oriented perpendicular to the foliation.

Clinopyroxene crystals in the veins or as interstitial grains display a weak orthorhombic CPO pattern, with [001] axes showing the strongest point concentration, which is usually subparallel to the orthopyroxene [001] maximum and to the olivine [100] maximum. The clinopyroxene CPO is thus coherent with those of olivine and orthopyroxene. In 12 samples, [100] axes are perpendicular to the foliation plane. In 6 other samples, [010] tends to be preferentially oriented normal to the foliation.

### 4.3.2 Transverse volcanic belt

### 4.3.2.1 Lashaine

Olivine CPO strength of Lashaine samples is more variable than for the rift axis peridotites. J-index ranges between 2 and 8 for those samples where more than 100 grains could be measured (Fig. 5). However, in some very-coarse grained peridotites, the number of measured grains was <100, leading to a possible overestimation of the J-index (Ben Ismail and Mainprice, 1997). These values are marked by dashed arrows in Fig. 5. Olivine CPO in

Lashaine peridotites varies from axial-[100] to axial-[010] patterns, with a predominance of orthorhombic patterns (BA indexes vary between 0.3 and 0.74, Fig. 5). Three samples (LS9, LS15, and 89-680) display axial-[010] CPO, characterized by a point concentration of [010] and a girdle distribution of [100] and [001] normal to it. Two samples (L1A and L1B, LS4A and LS4B) display orthorhombic CPO. In 2 other samples (89-664 and LS11), CPOs with a pattern intermediate between orthorhombic and axial-[100] are observed. In these rocks, the CPO is generally weak, but a point concentration of [100] and incomplete girdles of [010] axes are observed.

Orthopyroxene CPOs are more dispersed than olivine CPOs. They are characterized by a weak point concentration of [001] axes parallel to [100] of olivine. In most samples, [100] are parallel to [010] of olivine.

*4.3.2.2 Olmani*

The peridotites from Olmani display olivine CPO with variable strength (J-indexes vary between 2 and 9; Fig. 5). They show mainly axial-[100] to orthorhombic olivine CPO patterns (Fig. 5). Porphyroclastic samples tend to exhibit axial-[100] patterns, that is, higher olivine BA indexes, as well as higher J-indexes than granular samples. A single coarse-granular sample (89-772) is characterized by axial-[010] pattern.

When present, orthopyroxene has a CPO correlated to the olivine one. ¬¬In three samples, weak axial-[010] patterns can be observed (see Figure 5, sample OL3). They are characterized by a girdle distribution of [100] and [001] in the foliation plane and point concentration of [010] normal to it. The other samples display weak orthorhombic CPO symmetry (Figure 5, sample 03TZ14E1).

*4.4 Seismic properties*

Average anisotropic seismic properties for rift-axis and off-axis samples are illustrated in Fig. 6. To a first order, all localities share common seismological characteristics. The P-waves propagation is fastest close to the olivine [100] maximum, which corresponds to the lineation in the samples where it has been identified, and slowest close to [010] maxima, then normal to the foliation. The slowest propagation directions of the slow S-wave (S2) are in the YZ structural plane. The fast split shear wave (S1) is polarized in a plane containing the main concentration of olivine [100] and the propagation direction. The highest $Vp/Vs1$ ratio is also parallel to the preferred orientation of olivine [100] and the lowest $Vp/Vs1$ is observed for waves propagating normal to this direction.

Changes in olivine CPO symmetry result in second order variations of the seismic anisotropy pattern. Within the rift axis and at Olmani, where axial-[100] and orthorhombic olivine CPOs predominate, P-waves velocities are slow and S-waves azimuthal anisotropy is high within the YZ plane. The fastest velocities of S2-waves are observed for directions close to the lineation. The slowest propagation of the S1-wave occurs for directions either close or normal to the lineation, while the fastest S1 propagation are expected for directions at 45° to the lineation.
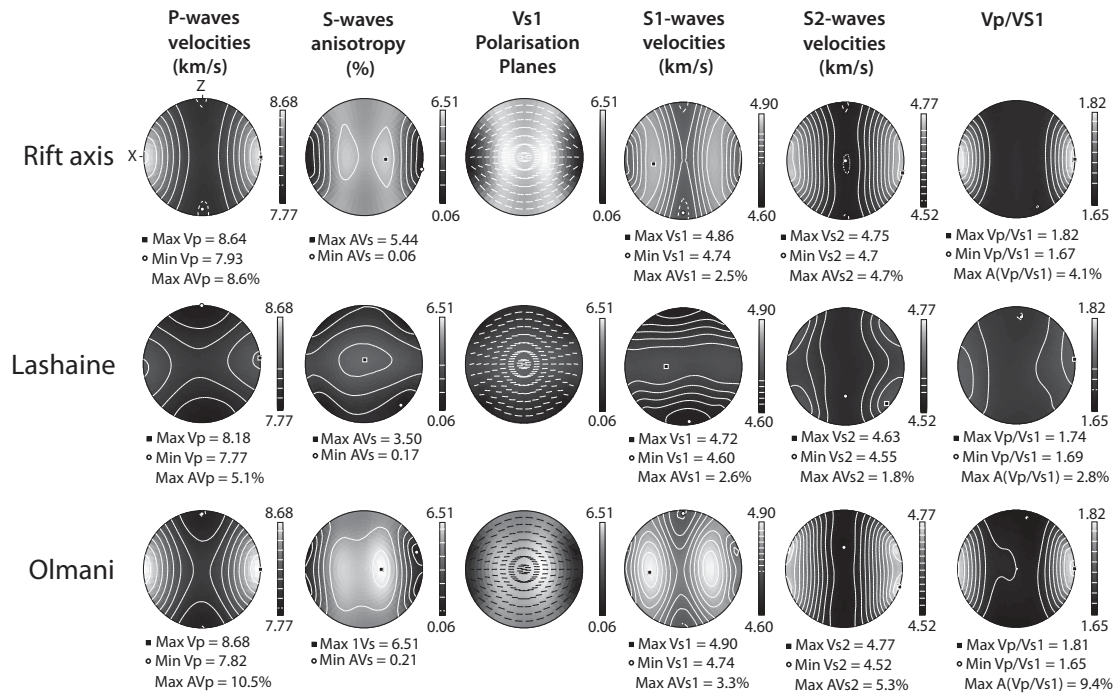


Figure 6: Calculated seismic properties of average samples for the rift axis, Lashaine, and Olmani localities. From left to right are displayed the 3-D distributions of P-wave velocities ($V_p$), S-wave polarization anisotropy ($AV_s$) and the orientation of fast shear wave polarization plane, $S_1$ wave velocities ($VS_1$), $S_2$ wave velocities, and $Vp/VS_1$ ratio. Black squares and white spots indicate maximum and minimum values, respectively.

At Lashaine, where axial-[010] to orthorhombic olivine CPOs dominate, slow P-waves velocities are found for propagation directions normal to the foliation plane. In contrast to the average properties computed for the rift axis, the S-waves polarization anisotropy is very low for propagation directions at high angle to the plane containing the concentrations of [100] and [001] (corresponding to the foliation when observed), with a minimum within the XZ plane at ~45° to the lineation. The maximum S-wave polarization anisotropy lies within the foliation at 90° to the lineation. The fastest propagation directions of $S_1$-wave are contained in the foliation plane, while the slowest directions are parallel to the Z structural

direction. Slow and fast S$_2$-waves propagation directions are observed in a plane normal to the lineation and in the XZ plane, at 45° to the lineation, respectively.

Seismic anisotropy intensities for individual samples are highly variable (Fig. 7, Table 1). Maximum P-waves anisotropies are comprised between 3.3 and 18.4%, while maximum S-waves polarization anisotropies range between 2.3 and 13.3 %. To a first order, both anisotropies display a weak positive correlation with olivine content (Fig. 7a-b). This is consistent with the observation that the presence of pyroxenes and garnet decreases the rock bulk anisotropy (Mainprice and Silver, 1993; Mainprice et al., 2000). Porphyroclastic peridotites, which have the strongest olivine CPO, tend to have the highest anisotropies, whereas granular peridotites yield the lowest anisotropies. Within a microstructural group, however, there is no systematic variation in anisotropy as a function of the provenance.
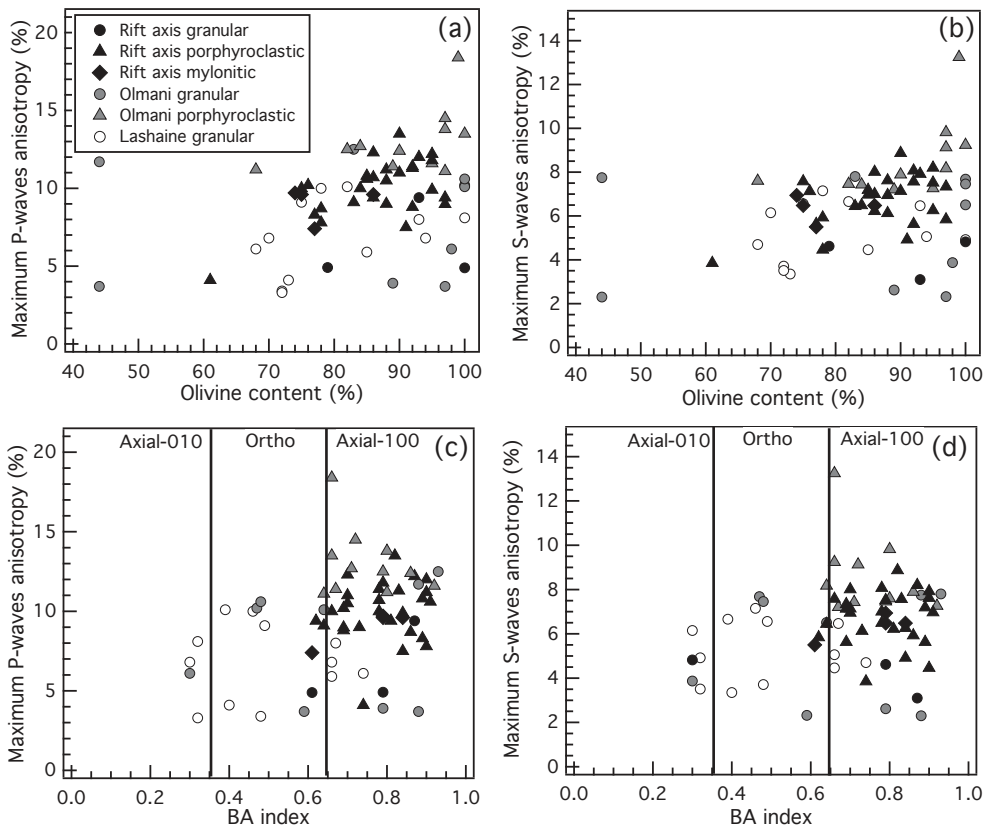


Figure 7: Dependence of the maximum P-wave anisotropy (AVp), and of the maximum S-wave polarization anisotropy (AVs) on the olivine content and the olivine CPO symmetry (BA index).

We observe no simple relationship between P- and S-waves anisotropy intensities and the olivine CPO symmetry (characterized by the BA index; Fig. 7 c, d). Most porphyroclastic peridotites, which have axial-[100] olivine CPO, are strongly anisotropic (Fig. 5), but their

large proportion of olivine and strong olivine CPO explain better their high anisotropy than the olivine CPO symmetry.

Crystallization of large volumes of metasomatic phases (>25% vol.) may considerably reduce P-, $S_1$- and $S_2$-waves velocities, and the maximum P- and S-waves anisotropy, as illustrated by Fig. 8, in which we compare the seismic properties of sample EL15 calculated by taking into account or not a phlogopite-bearing clinopyroxenite vein that crosscuts this sample. However, it has no effect on $Vp/VS_1$ and $Vp/VS_2$ ratios.
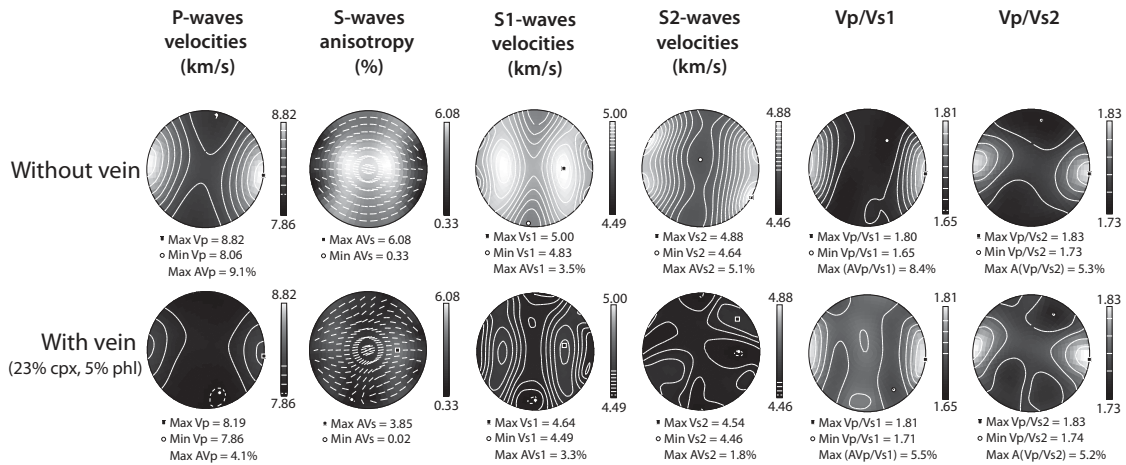


Figure 8: Effect of veins on the seismic properties of peridotite EL15 from Eledoi. From left to right are displayed the 3-D distributions of P-wave velocities ($V_p$), S-wave polarization anisotropy ($AV_s$) and the orientation of fast shear wave polarization plane, $S_1$ wave velocities ($VS_1$), $S_2$ wave velocities, and $Vp/VS_1$ and $Vp/VS_2$ ratios.

## 4.5 OH concentrations

### 4.5.1 Olivine

The olivine spectra of xenoliths from Pello Hill, Eledoi, Olmani, and Lashaine exhibit many absorption bands with highly variable intensities (Fig. 9a), suggesting H incorporation in a variety of point defects (Berry et al., 2005; Berry et al., 2007; Kovacs et al., 2010; Miller et al., 1987; Padron-Navarta et al., 2014). In a first group of samples (LS11, PEL41, 03TZ14J, EL6, PEL39), the absorption band at 3571 cm$^{-1}$ displays the maximum O-H absorbance, while the intensity of the absorption bands at 3596 and 3525 cm$^{-1}$ varies. Absorption bands between 3450 and 3200 cm$^{-1}$ have minor peaks, except for the band at 3226 cm$^{-1}$, which can be more developed. In a second group of samples (EL15a, PEL17, PEL7, PEL15), absorption bands between 3450 and 3200 cm$^{-1}$ present major peaks, with variable intensities. Finally, in a

third group of samples (PEL16, EL15b, 89-772, OL10, PEL40, PEL34), both absorption bands groups are observed.

### 4.5.2 Orthopyroxene and Garnet

Orthopyroxene spectra are more homogeneous (Fig. 9b) than those of olivine. They display up to seven absorption bands. The four major bands are found at 3600, 3544, 3517 and 3410 cm$^{-1}$. Their intensities are variable. Minor peaks are also present around 3473, 3324 and 3060 cm$^{-1}$.

Several millimeters long clear garnet grains were present in only one of the analyzed samples (harzburgite xenolith from Lashaine LS11). Their spectra are flat, indicating anhydrous garnet.
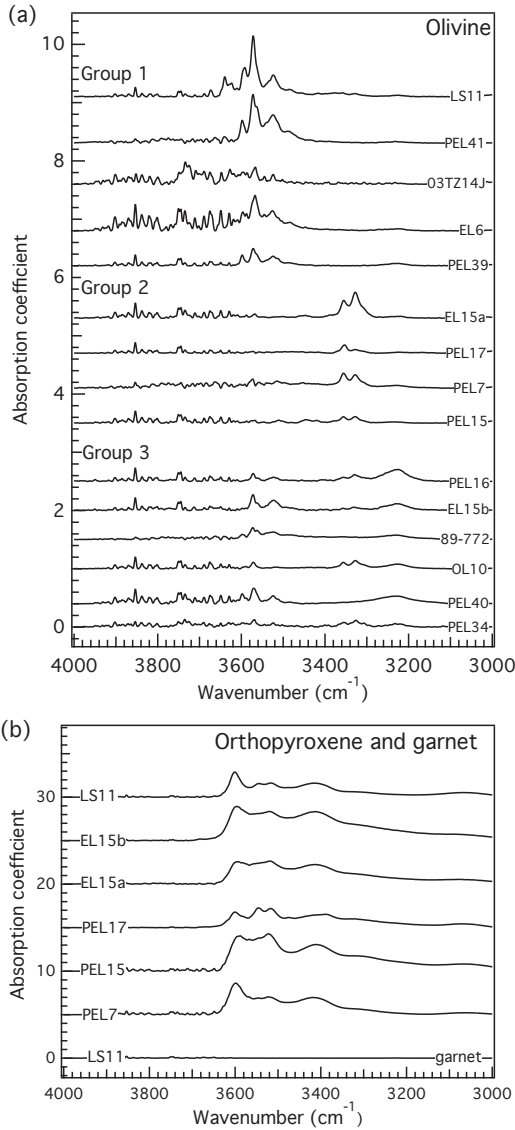


Figure 9: Representative unpolarized FT infrared spectra of nominally anhydrous minerals in xenoliths from Tanzania. (a) Olivine; (b) Orthopyroxene and garnet. All spectra are normalized to a sample thickness of 1 cm.
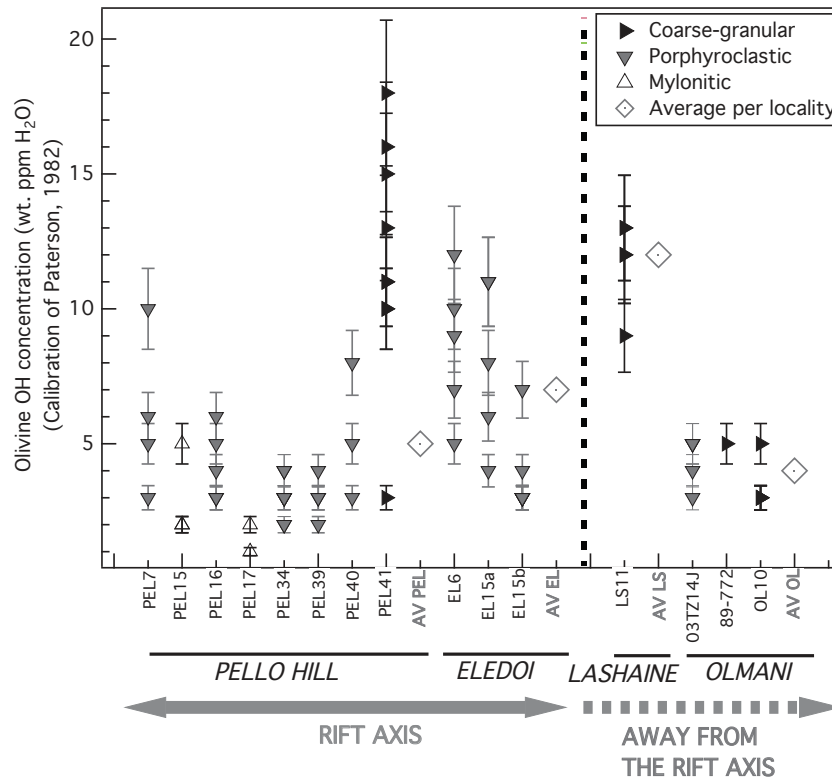
Figure 10: Representative unpolarized FT infrared spectra of nominally anhydrous minerals in xenoliths from Tanzania. (a) Olivine; (b) Orthopyroxene and garnet. All spectra are normalized to a sample thickness of 1 cm.

## 4.5.3 OH concentrations

Olivine OH concentrations are heterogeneous both between and within samples. They range between 2 and 12 wt. ppm $H_2O$ (Table 2, Fig. 10 and 11) and are in the range of concentrations previously measured for spinel peridotites (Denis et al., 2013; Falus et al., 2008; Grant et al., 2007; Kurosawa et al., 1997; Li et al., 2008; Peslier, 2010; Peslier and Luhr, 2006; Soustelle et al., 2010; 2013; Yang et al., 2008). Olivines from Pello Hill xenoliths are more heterogeneous than those from Olmani and Eledoi. However, there is no systematic correlation between olivine OH concentrations and provenance (Fig. 10). The lowest olivine OH concentrations are found in mylonites, in agreement with data from previous studies (Baptiste et al., 2012; Falus et al., 2008). The highest average olivine OH concentrations (12 wt. ppm $H_2O$) are observed in dunite PEL41 from Pello Hill and harzburgite LS11 from Lashaine. Although both samples are coarse-granular, in the whole set of analyzed samples, there is no systematic correlation between olivine OH concentration and microstructure. There is also no correlation between the olivine OH concentration and Mg# (Fig. 11).
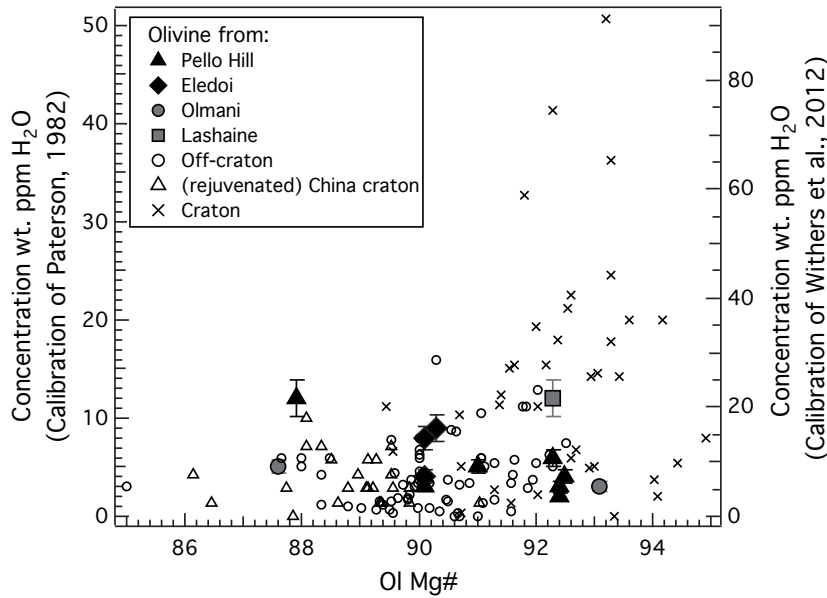
Figure 11: OH concentrations in wt. ppm H2O (calibration of Paterson, 1982) versus Mg# in olivine. For comparison, data obtained in previous studies on peridotite xenoliths from various localities are also shown (Baptiste et al., 2012; Demouchy et al., 2006; Denis et al., 2013; Falus et al., 2008; Grant et al., 2007; Kurosawa et al., 1997; Matsyuk et al., 1998; Matsyuk and Langer, 2004; Peslier and Luhr, 2006; Peslier et al., 2008; Peslier et al., 2010; Yang et al., 2008).

The homogeneity of OH concentrations in olivine was tested by profiles analyses with 50 to 150 μm step sizes along transect (850 to 3450 μm) on randomly oriented olivine grains in three samples: one mylonite from Pello Hill (PEL17), one garnet-bearing harzburgite from Lashaine (LS11), and one vein-bearing sample from Pello Hill (PEL41). These profiles indicate long homogeneous concentrations plateau within grains, incompatible with significant dehydration (Thoraval and Demouchy, 2014)

Average orthopyroxene OH concentrations range between 97 and 212 wt. ppm H2O (Table 2), being in the range of concentrations reported by previous studies (Falus et al., 2008; Peslier et al., 2002; Peslier, 2010). In rift axis samples, orthopyroxene OH concentrations are more heterogeneous, but there is no systematic correlation between orthopyroxene OH concentration and xenolith locality or microstructure. Indeed, the lowest orthopyroxene OH concentrations are measured in mylonite PEL17 and the highest, in mylonite PEL15. There is also no correlation between the olivine and orthopyroxene OH concentrations.

## 5. Discussion

*5.1 Thermomechanical and metasomatic evolution of North Tanzanian Divergence peridotites*

*5.1.1 Rift Axis (Pello Hill and Eledoi)*

The peridotites from the rift axis localities show a variety of microstructures, from mylonitic to porphyroclastic and coarse-granular. All exhibit evidence for plastic deformation and both dynamic and static recrystallization, but the deformation conditions and the extent of static recrystallization vary from one microstructure to another. The obliquity between the lineation and subgrain boundaries in olivine suggests simple shear deformation in both porphyroclastic peridotites and mylonites, but the higher elongation of orthopyroxenes and finer grain sizes imply deformation under higher stresses in the mylonites. The heterogeneity in microstructures may indicate a spatial or a temporal variation of deformation conditions and intensity within the mantle below Eledoi and Pello Hill.

In both mylonites and porphyroclastic peridotites, the frequency and spacing between subgrain boundaries in olivine porphyroclasts and the extent of grain boundary polygonization vary from sample to sample (Fig. 3a and b). These microstructural features support a deformation by dislocation creep followed by variable degree of annealing. The well-preserved intracrystalline deformation features in most porphyroclastic peridotites suggest, however, that the time span between the deformation and the extraction by the magma was too short to allow for complete annealing of the deformation microstructures. The recent character of the deformation is further supported by the rather high equilibration temperatures (1050-1100°C) recorded by these peridotites. The variable degree of annealing observed in these rocks may be explained by variable interaction with fluids or melts, by sampling of different depths, or by transient and spatially heterogeneous heating events.

Mylonites also record a temporal variation of deformation conditions. Highly stretched orthopyroxenes are a characteristic feature of the mylonites (Fig. 3a). Similar highly stretched orthopyroxenes have been described, in mylonitic peridotites from the Lanzo (Nicolas et al., 1972), Ronda (Tubìa et al., 2004; Soustelle et al., 2009), and Beni Bousera massifs (Frets et al., 2014), and were interpreted as the result of deformation under high stress at moderate temperatures (850-950°C estimated from thermobarometry in the peridotites and associated pyroxenites; Frets et al. 2014; Garrido et al. 2011). Closely spaced kinks in orthopyroxene also indicate deformation under high stress conditions. However, the stretched orthopyroxenes from the mylonites have indented shapes, with embayments filled by vein-like olivine crystals, which are often subparallel to the orthopyroxene elongation (Figure 4a).

In porphyroclastic peridotites, orthopyroxene embayments filled with olivine and olivine inclusions in orthopyroxene (Fig. 4c) are also present. These microstructures suggest reactions leading to consumption of orthopyroxene and crystallization of olivine. In both mylonites and porphyroclastic peridotites, the olivine crystals that replace orthopyroxene display ubiquituous undulose extinction and subgrain boundaries dominantly oriented normal to the crystals' elongation. This suggests that this reaction is synkinematic. Three processes may produce replacement of orthopyroxene by olivine: (1) incongruent melting of orthopyroxene (Kubo, 2002); (2) reaction between the peridotite and a Si-undersaturated melt (Kelemen et al., 1990, 1995), (3) percolation of aqueous fluids (Padrón-Navarta et al., 2010). The last process may occur at low temperatures (650-700°C), but implies very large volumes of aqueous fluids (Padrón-Navarta et al., 2010), which are plausible in a subduction zone, but not in a continental rift.

In summary, the recent deformation event recorded by the rift axis xenoliths started under high stress and probably low temperature. The deformation was later coupled with partial melting or reactive percolation of Si-undersaturated melts. Both processes imply high, near-solidus temperatures, which are at odds with the high stresses inferred in the mylonites from the stretching of orthopyroxenes. Moreover, the ubiquituous exsolutions seen in orthopyroxenes suggest significant cooling between this melt-assisted deformation and the extraction of the xenoliths. Together these observations imply transient and probably spatially heterogeneous temperature fields, marked by fast heating and cooling episodes, which probably accompanied deformation and reactive melt percolation. Interestingly, similar observations have been recently reported for peridotites samples from the boundary of the Middle Atlas (Marocco) in a context of progressive exhumation, leading to convergent interpretation (El Messbahi et al., in press).

Coarse-grained dunites (EL14, PEL11, and PEL41) contain more Fe-rich olivine in comparison to the other Tanzanian samples. In these rocks, subgrain boundaries are rare and triple junctions are common (Fig. 3e). They display, however, a clear crystallographic fabric. Altogether this suggests that efficient annealing followed deformation by dislocation creep. Dunite may form when a harzburgite interacts with Si-undersaturated melts (Berger, 1985; Berger and Vannier, 1984; Kelemen et al., 1990; Morgan and Liang, 2003). The coarse-grained dunites from Pello Hill and Eledoi contain olivines with significantly lower Mg# (84-88, while the average for the other microstructures in these localities is ~92, Table 1). Such a strong enrichment in Fe suggests interaction with very large volumes of melts. The coarse-grained dunites might represent melt channels or melt accumulation levels within the mantle

lithosphere (Berger, 1985; Berger and Vannier, 1984; Kelemen et al., 1995; Kelemen and Dick, 1995; Tommasi et al. 2004).

In mylonitic, porphyroclastic and coarse-granular peridotites, the well-defined olivine CPO indicates dislocation creep as the dominant deformation process. The olivine CPO patterns range from to orthorhombic. These olivine CPOs are consistent with deformation by simple or pure shear with dominant activation of (010)[100] or (0kl)[100] slip systems under high temperature, low pressure and anhydrous conditions (Tommasi et al., 1999; Tommasi et al., 2000). Axial-[100] CPO symmetry likely denotes a strain regime producing a well-defined stretching direction, such as transtension; Chatzaras and Kruckenberg (in press) have recently shown the correlation between axial-[100] CPO symmetry and prolate strain ellipsoids due to constructional deformation. Orthopyroxene CPOs indicate deformation by dislocation creep with activation of the [001](100) slip system. They are always correlated to the olivine CPO, indicating that both minerals underwent the same deformation event.

In addition to the olivine-forming reactive melt percolation, textural evidence for metasomatism by hydrous melts has also been identified in many peridotites from Pello Hill and Eledoi (see also Dawson and Smith, 1988, who first analyzed the composition of the veins from Pello Hill mantle xenoliths and concluded that they bear asthenospheric Nd and Sr isotopic signatures and imparted REE, K, Fe, Ti metasomatism on the surrounding peridotite). It encompasses: (1) veins with diffuse margins that comprise clinopyroxene, amphibole, phlogopite, and spinel that crosscut deformation microstructures (Fig. 3d), (2) irregularly-shaped pockets of clinopyroxene, amphibole, phlogopite, and spinel (Fig. 4e). In these minerals, deformation substructures are uncommon. However, clinopyroxene crystals in veins do exhibit a clear CPO that is coherent with the CPO of olivine and orthopyroxene from the surrounding peridotite. Two hypotheses may explain this observation. First, vein intrusion may be synkinematic, but this hypothesis is at odds with the orientation of the veins that crosscut the foliation and with the lack of plastic deformation of the metasomatic phases. Thus, we propose that the vein intrusion was post-kinematic and the minerals crystallized in a preferential orientation controlled by the orientation of the preexisting orthopyroxene.

### 5.1.2 Lashaine

Mantle xenoliths from Lashaine mainly display very coarse-grained microstructures characterized by millimeter- to centimeter-sized grains with curvilinear, interpenetrating boundaries and low densities of subgrain boundaries (Figure 3f, 4g). These observations point to efficient grain boundary migration. Together with the well-defined olivine and

orthopyroxene CPOs, they support deformation by dislocation creep at high temperature or effective annealing. In LS9, the frequent olivine-orthopyroxene interpenetrating boundaries suggest reaction with percolating melts. In addition, the olivine tablets growing on other crystals (Fig. 4f) have been previously interpreted as resulting from fast grain growth in presence of fluids (Drury and Van Roermund, 1989).

Among the studied samples, the xenoliths from Lashaine are the only ones containing garnet, implying that deeper parts of the Tanzanian lithosphere have been sampled. Garnet crystals in peridotites LS4 and LS11 display interstitial shapes and usually rim orthopyroxene. This morphology led Gibson et al. (2013) to interpret these pyrope garnets as the product of exsolution from orthopyroxene due to cooling.

Well-defined olivine and orthopyroxene CPOs in Lashaine peridotites indicate that dislocation creep was the main deformation process. Orthopyroxene CPOs are consistent with deformation by dislocation creep with dominant activation of [001](100), as usually observed in deformed mantle peridotites and pyroxenites (e.g., Frets et al. 2012, 2014; Vauchez et al., 2005). Olivine CPO patterns are dominantly orthorhombic to axial-[010] (Fig. 5). Axial-[010] olivine CPO symmetry, though less common than orthorhombic and axial-[100] symmetries (Tommasi et al., 2000), has been described in many xenoliths suites from continental and oceanic environments (e.g., Bascou et al., 2008; Tommasi et al. 2008; Vauchez et al., 2005; Zaffarana et al., 2014) and in peridotite massifs (e.g., Frets et al. 2014, Soustelle et al. 2010). It may result from similar activation of [100](010) and [001](010) slip systems as a result of changes in physical parameters (e.g., olivine water contents, pressure, differential stresses, presence of melt) during deformation or from a deformation regime characterized by an oblate strain ellipsoid (Chatzaras and Kruckenberg, in press) such as pure shear or transpression (Tommasi et al., 1999). A dispersion of olivine [100] axes has also been observed in rocks undergoing dynamic and static recrystallization (Falus et al., 2011; Tommasi et al., 2008). Experiments on olivine single crystals and polycrystals have shown that [001]-glide is favored at low temperature and high differential stresses (Demouchy et al., 2009; Demouchy et al., 2013; Demouchy et al., 2014; Durham and Goetze 1977; Phakey et al., 1972; Raleigh, 1968). However, this explanation is inconsistent with the very-coarse granular microstructures of Lashaine peridotites. The OH concentrations measured in olivine are too low (<20 wt. ppm H2O) to induce the transition from dominant [100] to dominant [001] glide suggested by Jung et al. (2006). Transition from [100] to [001] glide have also been observed as a result of increasing pressure in deformation experiments at high confining pressure (Couvy et al., 2004; Jung et al., 2006; Raterron et al., 2009). Occurrence of axial-

[010] CPO in garnet-bearing harzburgite LS11 may suggest a change in dominant mechanism with increasing pressure, an interpretation similar to the one proposed by Vauchez et al. (2005) for the deepest Labait peridotites. However, this explanation cannot account for the common axial-[010] patterns in the Lashaine spinel peridotites. Deformation in presence of melt, accompanied by refertilization reactions, also results in development of axial-[010] olivine CPO (Le Roux et al., 2008; Higgie et al., 2012, 2014). Yet, there is no clear evidence for synkinematic refertilisation reactions in the studied peridotites. Thus axial-[010] olivine CPO in Lashaine peridotites probably results from either transpression or recrystallization. Transpression should also result in dispersion of orthopyroxene [001] axes in the foliation plane, but the small number of orthopyroxene crystals present in most samples does not allow corroborating or excluding this hypothesis. Evidence for static recrystallization and grain boundary migration is, on the other hand, widespread in these peridotites.

### 5.1.3 Olmani

Xenoliths from Olmani display microstructures and CPOs intermediate between those found in peridotites from rift-axis localities and from Lashaine (Fig. 3 and 7). Half of the Olmani samples display coarse-grained to very coarse-grained sizes, similar to the microstructures observed in Lashaine. The other half of Olmani samples exhibits coarse-porphyroclastic to porphyroclastic microstructures, with characteristics similar to those observed in rift axis peridotites. All textural types from Olmani show evidence for olivine crystallization at the expenses of orthopyroxene. Chemical evidence for interaction with carbonatites was identified in several of the studied peridotites (89-772, 89-774, 89-776, and 89-773) by Rudnick et al. (1993). These samples display coarse-granular microstructures, suggesting that the carbonatitic metasomatism is not directly related to the recent deformation (probably rift-related), recorded by the porphyroclastic microstructures.

The well-defined olivine CPOs measured in Olmani peridotites suggests that dislocation creep was the main deformation process. All three olivine CPO symmetries are observed. Interestingly, Olmani granular peridotites tend to display axial-[010] olivine CPO, similar to those of the granular peridotites from Lashaine, whereas porphyroclastic to coarse-porphyroclastic samples show dominantly axial-[100] patterns, similar to rift axis peridotites. Moreover, the weak annealing observed in the porphyroclastic peridotites suggests that deformation occurred shortly before extraction. The orthopyroxene CPO is consistent with deformation by dislocation creep with dominant activation of [001](100) and [001](010) slip

systems. Olivine and orthopyroxene CPOs are always correlated, implying that they record the same deformation event.

A variation in microstructures and olivine CPO patterns between the localities of Olmani and Lashaine was not expected, as both localities are within the Tanzanian Divergence and distant of less than 30km. This variation may be explained by: (1) younger eruption ages in Olmani than Lashaine, in which case Olmani peridotites would record the recent deformation associated with the rifting, (2) a bias in xenolith sampling, (3) Olmani and Lashaine sample lithospheric domains with different tectonic ages, or (4) heteregeneous deformation of the lithospheric mantle at the scale of few tens of km within the transverse volcanic belt. The eruption age of Olmani and Lashaine is poorly constrained. However, neighboring volcanic centers with similar morphologies have eruption ages between 2.5-1.56 Ma (Evans et al., 1971; Le Gall et al., 2008; MacIntyre et al., 1974; Wilkinson et al., 1986). Hypothesis (1) is therefore improbable. A bias in xenolith sampling (2) cannot be definitely excluded, but is unlikely, since in spite of the large number of xenoliths collected, Lashaine xenoliths have very homogeneous microstructures. The presence of lithospheric domains of different ages (3) within the Mozambique belt is possible. Indeed, Lashaine and Olmani are located in a domain of the Mozambique belt that is interpreted as a remnant of cratonic lithosphere reworked during the Neoproterozoic Orogeny (Mansur et al., 2014; Möller et al., 1998). Similarities between Lashaine and cratonic peridotites are numerous. Rudnick et al. (1994) first highlighted similarities in mineral compositions between Lashaine and the Kaapvaal craton peridotites. Minimum ages of 3.4 and 2.9 Ga were obtained from Re-Os studies of sulphides in mantle xenoliths from both Lashaine and Labait, a Quaternary volcano located on the eastern boundary of the Tanzanian craton (Fig. 1; Burton et al., 2000; Chesley et al., 1999). Comparison of the microstructures and the olivine CPOs of the Labait and Lashaine peridotites provides additional evidence for a common origin. Vauchez et al. (2005) described three textural types in the Labait peridotites, among which the garnet-free, coarse-grained peridotites display microstructures and olivine CPO very similar to those observed in the Lashaine peridotites. However, the similarities between Lashaine and Olmani coarse-granular peridotites make hypothesis (3) unlikely. Heterogeneous rift-related deformation within the volcanic belt is the most probable explanation to Lashaine and Olmani microstructural and CPO difference. Indeed, the deformation recorded by the Olmani porphyroclastic peridotites might be related to localized deformation in a strain transfer zone connecting the main rift to the Pangani Graben (Fig. 1) or to reactivation of the

neoproterozoic Aswa shear zone (e.g., Corti et al., 2007; Ruotoistenmäki, 2014 and references therein) in a transtensional regime that resulted in the opening of the Pangani Graben.

*5.2 Hydration state of the Tanzanian lithosphere*

Diffusion data from experimentation and dehydration profiles from basalt-borne peridotite xenoliths, both point out to a very fast hydrogen ionic diffusion in olivine at high temperature (Mackwell and Kohlstedt, 1990; Demouchy and Mackwell, 2006; Demouchy et al., 2006; Peslier and Luhr, 2006; Denis et al., 2013). However, the length and homogeneity of OH concentrations plateau in olivine along profiles in three samples demonstrates that the measured concentrations were not modified during xenolith extraction (Demouchy et al., 2006; Thoraval and Demouchy, 2014).

Average OH concentrations in olivine measured in the Tanzanian samples vary from very low to moderate (up to 12 wt. ppm H2O; Fig. 10, Table 2). Average orthopyroxene OH concentrations range between 97 and 212 wt. ppm H2O. In xenoliths from Pello Hill, the olivine OH concentrations are more heterogeneous than in those from Eledoi and Olmani. However, this difference might be related to the fact that we analyzed more samples from Pello Hill than from other localities. We also observe no clear relationship between the microstructure or the olivine CPO pattern and OH concentrations (Table 2, Fig. 10). We also do not observe significant differences in olivine OH concentrations between in- and off-axis samples (Fig. 10). The 2 samples that exhibit the highest OH concentrations in olivine, are a garnet-bearing harzburgite LS11 from Lashaine and a vein-bearing dunite PEL41 from Pello Hill. We discuss below the potential origin of these relatively higher OH concentrations.

The harzburgitic to dunitic compositions, and high olivine Mg# in most samples suggest extensive partial melting, which might be as old as 3.4 Ga, based on Os isotopic dating of sulphides in a garnet lherzolite from Lashaine (Burton et al., 2000). Since H behaves as an incompatible element during partial melting (Bolfan-Casanova, 2005; Dixon et al., 2002; Hirschmann et al., 2005), olivine with high Mg# should have the lowest OH concentrations. However, we observe no correlation between olivine Mg# and OH concentrations (Fig. 11), implying that the Tanzanian samples were potentially hydrated or rehydrated during later metasomatic events.

Geochemical studies have provided evidence for multiple metasomatic events in mantle xenoliths from the sampled localities. Carbonatite metasomatism led to enrichment in REE, increase in Mg#, and the crystallization of clinopyroxene and phosphate in Olmani xenoliths (Rudnick et al. 1993, 1994). However, this carbon-rich metasomatism should not

result in extensive hydration of Nominally Anhydrous Minerals (NAM) because a high CO2 fugacity will lower H2O fugacity in the system and thus minimize the hydration of NAMs (Dixon et al., 1995, Sokol et al., 2010). In Lashaine peridotites, an episode of metasomatism, which enriched the peridotites in K, Fe Ca, Ti, Rb and REE, was dated at ~2 Ga based on Re-Os isotope data on sulphides (Burton et al., 2000; Dawson, 2002). A more recent metasomatism led to addition of Si, K, Ti, Ca, Fe, Nb, and Ta (Dawson, 2002). Rudnick et al. (1994) suggested that the SiO2 enrichment in Lashaine garnet peridotites was caused by the interaction with silicic melts derived from partial melting of a subducting slab, during the major subduction on the eastern edge of the Kaapvaal craton around 2 Gy ago (Möller et al., 1995). Such a process may modify the trace element contents of NAMs and therefore allow for OH incorporation in olivine. It might therefore explain the relatively high OH concentration in olivine from garnet-bearing harzburgite LS11 (Fig. 10). Moreover, LS11 harzburgite is a garnet-bearing peridotite. Its deeper origin may also explain the higher OH concentration, since higher pressure implies higher water fugacity, favoring OH incorporation in olivine (Kohlstedt et al., 1996; Férot and Bolfan-Casanova, 2012).
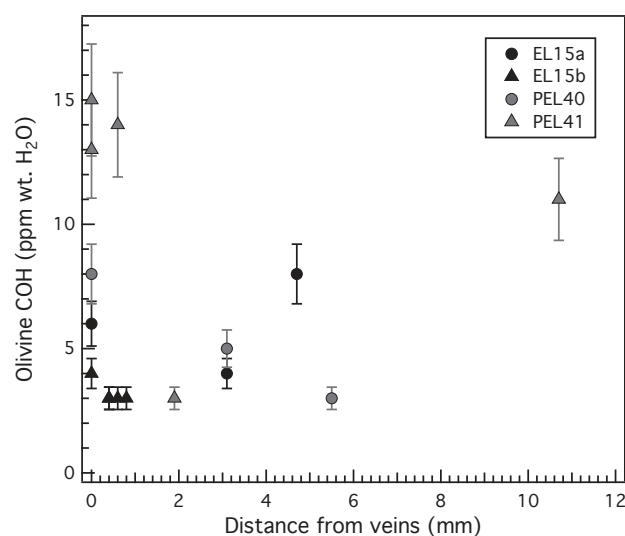


Figure 12: Olivine OH concentrations in wt. ppm $H_2O$, (calibration of Paterson, 1982) as a function of the distance from hydrous mineral-rich veins.

The presence of undeformed hydrous phases in veins or diffuse pockets (Fig. 3d, 4d,e) in xenoliths from all sites implies extensive post-kinematic metasomatism by hydrous fluids or melts. Indeed, the vein-bearing dunite PEL41 from Pello Hill shows the highest OH concentrations in olivine from all analyzed samples (Fig. 10). However, measurement of the OH concentration in olivine at different distances from the veins in dunite PEL41 shows no systematic increase in olivine OH concentrations in the vicinity of the vein (Fig. 12). Similar

measurements were performed for samples EL15 and PEL40. These data suggest that hydration of olivine is not related to the metasomatic event that formed the veins. The actual nature of the metasomatic agent and the timing of the hydration of olivine remain therefore undetermined.

*5.3 Upper mantle deformation and seismic anisotropy in the North Tanzanian Divergence*

Microstructures and CPOs analysis of the Tanzanian xenoliths show that the lithospheric mantle in the Northern Tanzanian Divergence is pervasively deformed. However, the strong heterogeneity in microstructures and olivine CPO suggests that this deformation was acquired during multiple tectonic events, probably separated by quiescence episodes, which allowed for annealing. The observed microstructural heterogeneity could also be explained by spatial variations in strain rate. The mylonitic to granular microstructures of the rift axis peridotites, despite rather high equilibrium temperatures, underwent limited annealing, which suggests that they were deformed shortly before extraction. Therefore, these samples likely record the deformation associated with the rift propagation in this region. Among the peridotites from the rift axis, the most common olivine CPO pattern is the axial-[100] pattern. This pattern implies that: (1) [100] is the dominant glide direction in olivine and (2) the active deformation regime has a well-defined stretching direction. Numerical models show that development of axial-[100] olivine CPO is characteristic of transtensional deformation regimes (Tommasi et al., 1999). High temperature (1200°C), high strain rate ($<10-6$ s-1) torsion experiments in dry olivine aggregates (Bystriky et al., 2000; Hansen et al. 2014) have shown, however, that [100]-axial CPO also forms during the initial stages of simple shear deformation, with a progressive transition from axial-[100] symmetry to orthorhombic symmetry for $\gamma > 5$. The obliquity between subgrain boundaries and the foliation observed in the mylonites and porphyroclastic peridotites are consistent with a simple shear component of deformation. In addition, the extreme stretching of the pyroxenes in the mylonites (Fig. 3a, 4a) implies high finite strains. Altogether, these observations support that the deformation, which developed the mylonites and porphyroclastic peridotites in the mantle lithosphere beneath the southern part of the East-African rift, results from a transtensional strain regime with a strong simple shear component.

Comparison between the seismic properties of the studied xenoliths and seismological data may help to further constrain the deformation regime in the region (e.g., Vauchez et al., 2000). Anisotropy measurements in the Tanzania Divergence show fast SKS polarization directions parallel or slightly oblique to the rift axis (Albaric et al., 2014; Bagley and

Nyblade, 2013; Gao et al., 1997; Walker et al., 2004). Oblique fast polarization directions for teleseismic shear waves are expected for a rift formed by transtensional deformation of the lithosphere, which should result in axial-[100] olivine CPO patterns with a concentration of olivine [100] axes close to horizontal and slightly oblique to the rift axis (Vauchez et al., 2000). These data, together with the predominance of axial-[100] olivine CPO in the studied mantle xenoliths from Pello Hill and Eledoi, are in good agreement with the suggestion that the East African Rift was initiated by a transtensional reactivation of inherited crystallographic fabrics, as suggested by Tommasi and Vauchez (2001) and Tommasi et al. (2009) who showed, using numerical models, that a CPO-induced mechanical anisotropy in the mantle imposes deformation with a strong strike-slip component parallel to the reactivated mantle structure.

Away from the rift axis, the coarse-granular, highly annealed microstructures of the Lashaine peridotites probably record an older deformation event. The olivine CPO in these peridotites also differ markedly from those from the rift axis: axial-[010] to orthorhombic patterns predominate. The deformation microstructures and CPOs frozen in these peridotites might be related to the last major compressive event in the region: the formation of the Mozambique Belt during the Neoproterozoic East African Orogeny (e.g., Pinna et al., 1993). Considering the similarity in microstructure and composition between the xenoliths from Lashaine, Labait (Vauchez et al. 2005), and the Kaapvaal craton (Baptiste et al. 2012), it may also be hypothesized that the lithosphere beneath Lashaine is a remnant of a cratonic domain embedded and preserved in the Mozambique Belt, as suggested by Gibson et al. (2013) from the geochemical study of ultra-depleted garnets. In this case, the structures and CPO of Lashaine xenoliths might result from even older deformations, such as those recorded in the neighboring Tanzanian craton (e.g., Bagley and Nyblade, 2013; Walker et al., 2004). Although localized within the transverse volcanic belt, the Olmani mantle xenoliths show both types of microstructures and CPOs: rift-axis or Lashaine ones. This might result from localized deformation reworking an older lithosphere (similar to the Lashaine mantle, or affected by the Aswa transcurrent shear zone) leading to the development of a subordinate branch of the East African Rift southeast of Mount Kilimandjaro (see Fig. 1).

The present study shows that lithospheric mantle beneath the southern part of the East African Rift is anisotropic. Below the rift axis, calculated seismic anisotropy intensities (Fig. 7, Table 1) range between 3.3 and 18.4% for P-waves, and between 2.3 and 13.3 % for S-waves. The contribution of the mantle lithosphere cannot therefore be neglected in the interpretation of shear wave splitting data, even if the coherence of the large-scale seismic

anisotropy pattern has lead investigators to favor a sublithospheric flow interpretation (e.g., Bagley and Nyblade, 2013). Estimates of the crustal and lithospheric thicknesses in this region vary between 36-44 km and 100-150 km (Dugda et al., 2009; Julià et al., 2005), respectively. Upper mantle S-wave velocities of 4.6 km/s were measured in the region (Julià et al., 2005). Assuming that the rift formed by transtension, we expect the foliation to be near vertical and the lineation close to horizontal and slightly oblique to the rift axis (Vauchez et al., 2000). SKS-waves will then sample the maximum S-wave polarization anisotropy (Z direction in Fig. 6), leading to delay times around 0.65s for a 60 km-thick mantle, and of 1.2s for a 110 km-thick mantle. In the North Tanzanian Divergence, Walker et al. (2004) measured SKS delay times of 0.3-0.8s, while Bagley and Nyblade (2013) and Albaric et al. (2014) obtained mean delay times of 0.7 and 1.2s, respectively. Therefore, the anisotropy induced by olivine CPOs in the Tanzanian peridotites can explain the SKS delay times measured in the region. Within the main Ethiopian rift, SKS studies also report polarization directions subparallel to the rift trend and variable delay times (0.5-1.7s: Gashawbeza et al., 2004, 1-3 s: Kendall et al., 2005). However, SKS splitting delay times as high as those reported by Kendall et al. (2005) in the Afars, cannot be explained by the anisotropies recorded in Tanzanian xenoliths, in agreement with the interpretation that they reflect the presence of oriented melt pockets (Ayele et al., 2004; Bastow et al., 2010; Hammond, 2014; Kendall et al., 2005; Sicilia et al., 2008).

## 6. Conclusions

Xenoliths sampling the lithospheric mantle beneath the North Tanzanian Divergence in the East African Rift display a high variability in microstructures and olivine CPO depending on their location. Beneath the rift-axis and Olmani, within the volcanic transverse belt, the occurrence of mylonitic to porphyroclastic microstructures suggests recent deformation by dislocation creep. Variable microstructures and grain sizes in these rocks suggest lateral and/or vertical variation of the deformation conditions within the mantle, as well as variable degrees of annealing, that may be related to variable interaction with fluids or melts, or to different time spans between deformation and xenolith extraction. The presence of mylonites point to strain localization, but there is no evidence of dominant grain boundary sliding in any of the studied rocks: the ubiquitous dislocation-related intracrystalline deformation features in olivine and orthopyroxene and the strong axial-[100] olivine CPO point to dislocation creep with dominant activation of the [100](010) slip system. The mylonites also record evidence for marked changes in temperature, probably due to transient

heating events. Highly stretched orthopyroxene crystals in mylonites from rift axis localities suggest that the deformation initiated under high stress and probably low/moderate temperature conditions, but the evidence of synkinematic olivine crystallization at the expenses of orthopyroxene observed in both mylonitic and porphyroclastic peridotites from rift axis localities and Olmani indicate that deformation continued in the presence of melt, under near-solidus conditions. Finally, ubiquitous exsolutions in orthopyroxene in the mylonites suggest significant cooling between this melt-assisted deformation and the xenoliths extraction. Late, postkinematic metasomatism by hydrous melts is evidenced by the occurrence of veins crosscutting the microstructure, as well as the presence of interstitial clinopyroxene and phlogopite in rift axis peridotites.

In the volcanic transverse belt, the coarse-granular microstructures and well-defined CPOs that characterize the Lashaine and part of the Olmani peridotites likely result from an older deformation event. The well-defined axial-[010] to orthorhombic CPO patterns in these peridotites may be associated with the formation of the Mozambique Belt or with an even older event. Finally, the variability of microstructures and CPOs in Olmani peridotites, which are either Lashaine-like or rift-axis-like, may indicate a heterogeneous deformation within the volcanic transverse belt, probably related to localized deformation associated to the development of the Pangani Graben through transtensional reactivation of the Aswa shear zone (Fig. 1).

Tanzanian xenoliths are variably hydrated (OH contents in olivine vary between 2 and 18 ppm H2O wt., Paterson calibration), but olivine OH concentrations do not vary systematically neither between in- and off-axis samples, nor as a function of the microstructure or CPO patterns. Occurrence of OH in olivines with high Mg# implies hydration by metasomatism after partial melting. However, the lack of spatial correlation between OH contents in olivine and the veins containing hydrous phases, implies that the olivine hydration is not directly due to the vein-forming metasomatism.

Maximum P wave azimuthal anisotropy (AVp) ranges between 3.3 and 18.4% and the maximum S wave polarization anisotropy (AVs), between 2.3 and 13.2%. The change in olivine CPO symmetry from a locality to another results in a variation in the seismic anisotropy patterns. Comparison between olivine CPOs and polarization direction of the fast SKS wave is consistent with a rift formed by a transtensional deformation involving reactivation of inherited tectonic fabric.

## Acknowledgments